

Masterarbeit

Studies on the Epitaxial Growth of Ultrathin Metal Oxide Films

Ralph Buß

12. Juni 2015

Erstprüfender: Prof. Dr. Joachim Wollschläger

Zweitprüfender: Dr. Karsten Küpper

Abstract

For spintronic devices, such as magnetic tunnel junctions (MTJs), ultrathin Fe_3O_4 films show promising properties for the use as ferromagnetic electrodes. So far, MgO is used as support for Fe_3O_4 films, but it shows unwanted diffusion behaviour in the production process. SrTiO_3 (STO) has been introduced as a replacement for MgO , although it does not have ideal qualities for epitaxial growth of Fe_3O_4 films.

This work studies the growth behaviour of ultrathin Fe_3O_4 films on $\text{STO}(001)$ supports by stepwise deposition, as well as the diffusion behaviour in $\text{Fe}_3\text{O}_4/\text{NiO}/\text{STO}(001)$ systems at different annealing temperatures. XPS and LEED experiments are used for the studies. It is observed that Fe_3O_4 tends to grow in (001) oriented epitaxial islands on $\text{STO}(001)$, with an (111) oriented epitaxial interface layer. Closed Fe_3O_4 films can be achieved at low sample temperatures and with high deposition rates. Annealing of the $\text{Fe}_3\text{O}_4/\text{NiO}/\text{STO}(001)$ systems show no indications of diffusion below 400°C . Above that temperature diffusion of Fe and Ni are observed, possibly leading to the formation of NiFe_2O_4 .

Kurzfassung

Ultradünne Fe_3O_4 Schichten zeigen vielversprechende Eigenschaften für die Verwendung als ferromagnetische Elektroden in spintronischen Bauelementen, wie zum Beispiel magnetischen Tunnelkontakten (MTJ). Oft wird MgO als Trägermaterial für Fe_3O_4 Schichten verwendet. Dieses zeigt aber unerwünschtes Diffusionsverhalten im Produktionsprozess. Die Verwendung von SrTiO_3 (STO) stellt eine Alternative zu MgO Substraten da, obwohl es keine idealen Eigenschaften für das epitaktische Wachstum von Fe_3O_4 Schichten aufweist.

Diese Arbeit untersucht das Wachstumsverhalten ultradünner Fe_3O_4 Schichten auf $\text{STO}(001)$ Trägermaterial durch schrittweises Aufdampfen, sowie das Diffusionsverhalten in $\text{Fe}_3\text{O}_4/\text{NiO}/\text{STO}(001)$ Schichtsystemen bei verschiedenen Nachheiztemperaturen. Zur Untersuchung der Proben werden XPS und LEED Messungen durchgeführt. Für das Wachstum von Fe_3O_4 auf $\text{STO}(001)$ wird die Bildung einer (111) orientierten epitaktischen Zwischenschicht beobachtet, auf der (001) orientierte epitaktische Inseln wachsen. Geschlossene Fe_3O_4 Schichten können durch niedrige Temperaturen und hohe Aufdampfzeiten erreicht werden. Das Nachheizen von $\text{Fe}_3\text{O}_4/\text{NiO}/\text{STO}(001)$ Schichtsystemen zeigt keine Hinweise auf Diffusion bei Temperaturen unterhalb von 400°C . Oberhalb dieser Temperatur wird die Diffusion von Fe und Ni beobachtet, die möglicherweise zur Bildung von NiFe_2O_4 führt.

Contents

1	Introduction	7
2	Thin Films	9
2.1	Growth of Thin Films	9
2.2	Solid State Diffusion	11
3	Experimental Methods	13
3.1	X-Ray Photoelectron Spectroscopy	13
3.1.1	Qualitative Analysis of Photoelectron Spectra	14
3.1.2	Quantitative Analysis of Photoelectron Spectra	15
3.1.3	Identification of Growth Modes using XPS	17
3.2	Low Energy Electron Diffraction	18
3.2.1	Facets	20
4	Materials and Sample Preparations	21
4.1	Strontium Titanate	22
4.2	Magnetite	22
4.3	Nickel Oxide	24
5	Growth of Ultrathin Fe₃O₄ Films on STO Support	25
5.1	Experimental Setup	25
5.2	Determination of Film Thickness and Stoichiometry	26
5.3	Determination of Growth Modes	28
5.4	Determination of Film Structures	31
5.5	Discussion	32
6	Interlayer Diffusion in Post Deposition Annealing	35
6.1	Sample Preparation	35
6.2	Experimental Setup	37
6.3	Surface Analysis	38
6.4	Analysis of the Surface Near Layers	40
6.5	Depth Profiling	43
6.6	Discussion	48
7	Conclusion	51
	Bibliography	53

1 Introduction

In materials science, thin films — solid layers with thickness's of typically less than $10\ \mu\text{m}$ — play an important role in applications such as optical and hard coating, as well as in microelectronics [2]. But, not only since microelectronics made the step towards nanoelectronics, the properties of structures with thickness's below $100\ \text{nm}$, i.e. ultrathin films [26], have become of great interest as on these scales new physical effects and phenomena emerge [38].

Spintronics (spin transport electronics) is one highly discussed field in research and development of electronics, where ultrathin films are of great importance. In contrast to conventional electronics, where information is processed by charge transport, in spintronics information is carried by the spin of electrons. The traditional approach in spintronics to process information is by alignment of the spin (“up” or “down”) relative to a reference, that could be an applied magnetic field or the magnetization of a ferromagnetic film. Spintronic devices are believed to lead to great advances in data processing speed, power consumption and integration density compared to conventional semiconductor devices [39].

One prominent research topic in spintronic devices are magnetic tunnel junctions (MTJs). These devices operate on the giant magnetoresistive effect and are made up of two ferromagnetic layers separated by an insulating tunnel barrier. Depending on the relative orientation of the magnetization of the two ferromagnetic layers, the resistance across the MTJ changes due to spin-dependent tunneling through the insulating layer. Parallel orientation of the magnetization results in low resistance, while antiparallel orientation results in high resistance. To be able to change the magnetic orientation of the two layers independently, ferromagnetic layers with different coercitivities are used. One common option is to magnetically pin one of the ferromagnetic layers by exchange bias with an anti-ferromagnetic layer (e.g. NiO) [20].

Ultrathin Fe_3O_4 films have been proposed as ferrimagnetic spin injectors due to the theoretically predicted 100% spin polarization at the Fermi energy [23]. Because of a small lattice misfit of only 0.3%, MgO has been used as insulating support for thin film growth of Fe_3O_4 [5, 6], but it has been shown, that interdiffusion of Mg caused by necessary annealing in the production process of MTJs is a great problem [14]. Recent work [11] has proposed SrTiO_3 (STO) as an interesting alternative as support for growth of ultrathin Fe_3O_4 films, although the quite large lattice misfit of 7.5% for Fe_3O_4 poses a problem for epitaxial growth of smooth layers.

Therefore, this work studies in a first part (chapter 5) the growth of ultrathin Fe_3O_4 films on STO(001) supports and in a second part (chapter 6) annealing effects in $\text{Fe}_3\text{O}_4/\text{NiO}/\text{STO}(001)$ systems. These studies are mainly done by XPS and LEED experiments, to which an introduction is given in chapter 3. Thin film growth and

solid state diffusion are shortly explained in chapter 2, while the main properties of the studied materials are summarised in chapter 4.

2 Thin Films

Thin films are defined as solid layers, that are created by deposition of atoms, molecules, or ions one-by-one (i.e. grown) on a solid surface (substrate) [2]. The term monolayer (ML) is often used to describe the amount of material needed to completely cover a surface with one layer of atoms. For complex compounds this may refer to molecules or basic clusters instead of atoms.

2.1 Growth of Thin Films¹

This thesis concentrates in particular on heteroepitaxial growth, in which both, substrate and film, form crystalline structures, but consist of different materials. How well a film can grow on a substrate thereby depends on the differences in lattice structure and lattice constant of the interfacing lattice planes. This is commonly indicated by the lattice misfit

$$\epsilon = \frac{b_0 - a_0}{a_0} \quad (2.1)$$

of the lattice constants b_0 of the film and a_0 of the substrate.

In homoepitaxy or rare cases of heteroepitaxy, where there is no lattice misfit between film and substrate, the film will tend to perfectly replicate the substrate lattice as is shown in Fig. 2.1a. However, even a small lattice misfit will result in pseudomorphic growth, where the film does not grow according to its bulk lattice, but adapt to the substrate lattice in the lateral plane. To minimize energy, the film will grow with an also distorted vertical lattice parameter (Fig. 2.1b). This adaptation introduces strain

¹For this section the book of Oura et al. [25] has been used as reference.

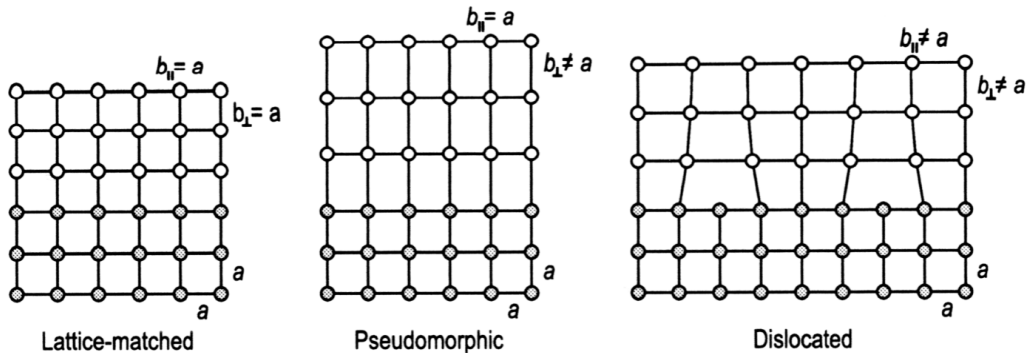


Fig. 2.1: Schematic representation of heteroepitaxial growth: (a) lattice-matched, (b) pseudomorphic, and (c) dislocated. Image taken from Oura [25, p. 378].

to the film, which will be even greater, the larger the lattice misfit is. A mechanism to relieve this strain is the formation of dislocations as Fig. 2.1c shows. This will result in the relaxation of the film with increasing thickness, leading to a more bulk-like structure in lattice planes further away from the substrate.

To describe thin film growth from a more macroscopic perspective, abstracting from the many atomic processes involved, the idea of surface energy or surface tension has been used [21]. Considering the film as a drop of liquid on the plain surface of a substrate, as shown in Fig. 2.2, one can identify three tensile forces acting on the contact point of film and substrate: The surface tensions γ_S and γ_F of substrate and film, respectively and the tension of the interface between film and substrate $\gamma_{F/S}$. With the wetting angle φ , the equilibrium condition of these forces can be written as

$$\gamma_S = \gamma_{F/S} + \gamma_F \cos(\varphi). \quad (2.2)$$

As considerations using the surface energy come to an equivalent result and to comply with common literature, in the following the term surface energy will be used instead of surface tension.

From equation (2.2) two different modes of thin film growth can directly be deduced. If the surface energy of the substrate is greater than the combined surface energies of film and interface,

$$\gamma_S \geq \gamma_{F/S} + \gamma_F, \quad (2.3)$$

the film will completely wet the substrate and thus one epitaxial layer will be completely closed, before the next starts to grow. This layer-by-layer growth, which is also referred to as Frank-van der Merwe growth, is shown in Fig. 2.3a. The second growth mode appears, if the surface energy of the substrate is less than that of film and interface,

$$\gamma_S < \gamma_{F/S} + \gamma_F. \quad (2.4)$$

Then the film will avoid covering the substrate and instead growth of epitaxial islands (Vollmer-Weber growth) takes place, as is shown in Fig. 2.3c. A third growth mode is the Stranski-Krastanov or layer plus island growth, which is shown in Fig. 2.3b. This growth mode starts as layer-by-layer growth, as condition (2.3) is initially fulfilled. But after a few layers have formed, islands start to grow on top of these layers, as the values for γ_F and $\gamma_{F/S}$ have changed, due to relaxation processes in the film, making island growth energetically more favourable, as now condition (2.4) is fulfilled.

In reality, the considerations about surface energies can only give hints on what growth mode to expect for a certain materials system, as the growth kinetics of adsorption, desorption, surface diffusion and nucleation (in detail described e.g. in Oura et al. [25]) are much more complicated. Besides the surface energies of the materials involved, such parameters as sample temperature and deposition flux play an important role.

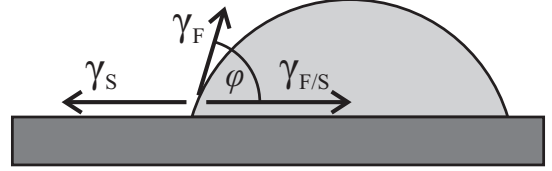


Fig. 2.2: Schematic showing a film island on a substrate with tensile forces γ and wetting angle φ .

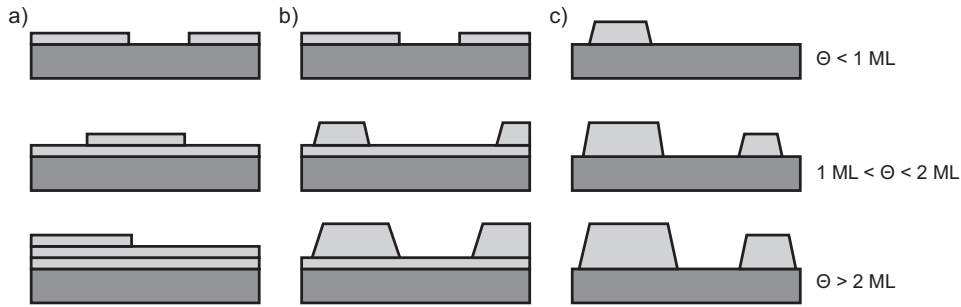


Fig. 2.3: Schematic representation of the three main growth modes at different coverages Θ : (a) layer-by-layer growth, (b) layer plus island growth, and (c) island growth.

2.2 Solid State Diffusion²

Diffusion in solid matter is hindered by the fact that atomic movement is constrained by the surrounding lattice structure. The transition of an atom from one lattice site to another requires first of all the formation of a vacant neighbouring lattice site and second, the atom has to overcome the energy barrier between the two lattice sites. Both processes require certain activation enthalpies, resulting in an effective energy barrier Q for the complete transition process. There are several possible ways atoms can move to a neighbouring lattice site, but according to Gottstein [15] it has been shown that the vacancy mechanism is the most probable, as its effective energy barrier is the smallest.

Solid state diffusion can thus be described as a thermally activated jump motion, where the diffusion coefficient

$$D = \frac{\lambda^2}{6} \Gamma \quad (2.5)$$

depends on the jump distance λ and the jump frequency

$$\Gamma = \nu \exp(-Q/kT). \quad (2.6)$$

The jump frequency is interpreted such that an atom tries to overcome the effective energy barrier to a neighbouring lattice site ν times per second, succeeding with a probability given by the Boltzmann factor $\exp(-Q/kT)$. The attack frequency ν is assumed to be equal to the atomic vibration frequency, i.e. $\simeq 10^{13} \text{ s}^{-1}$. As the jump distance and the height of the effective energy barrier depend on the lattice structure and the type of atom, the diffusion coefficient and thus the speed of diffusion can vary greatly for diffusion of different elements in various materials.

This kind of diffusion in the bulk volume of solid matter is practically frozen at lower temperatures as the thermal energy of atoms becomes insufficient to overcome the effective energy barrier. A process that allows for more rapid diffusion, even at lower temperatures, is diffusion along grain boundaries and dislocation lines. As these are already made up of vacant lattice sites, there is no formation energy needed for the transition of atoms between lattice sites and the effective energy barrier is greatly

²For this section the book of Gottstein [15] has been used as reference.

reduced. The diffusion coefficient for grain boundary diffusion thus depends more on the structure of the grain boundary, than on the material the solid is made up of [15].

3 Experimental Methods

This chapter gives a short introduction to the two main experimental techniques used in this work: X-ray photoelectron spectroscopy and low energy electron diffraction.

3.1 X-Ray Photoelectron Spectroscopy¹

X-Ray Photoelectron Spectroscopy (XPS) is a mainly surface sensitive technique, developed for chemical analysis. The basic experimental setup is pictured in Fig. 3.1a. It consists of an X-ray source, an energy discriminative electron analyser, an electron detector and the sample, contained in an ultra high vacuum (UHV) chamber (i.e. $p < 10^{-9}$ mbar). X-rays of a specific energy $h\nu$ (excitation energy) are utilised to induce the emission of electrons from the sample, creating vacancies with binding energy E_b . The photoelectrons are projected through an electron lens and a hemispherical analyser onto the detector and are counted according to their kinetic energy. As both, sample and analyser have work functions Φ_S and Φ_A , respectively, photoelectrons registered by the detector with kinetic energy E_{kin} have been bound in the sample with binding energy

$$E_b = h\nu - E_{kin} - \Phi_A, \quad (3.1)$$

as is demonstrated in Fig. 3.1b. The spectrum of photoelectrons is displayed as intensity (counts per second, cps) over binding energy E_b . The value of the unknown analyser work function Φ_A is empirically determined by calibration to the Fermi edge of a reference sample or to a well known peak in the spectrum. The latter can also compensate for unequal Fermi energies E_F of sample and analyser due to charging of poorly-conducting samples.

line	energy shift (in eV)	relative intensity (in %)
K _{α3}	9.8	6.4
K _{α4}	11.8	3.2
K _{α5}	20.1	0.4
K _{α6}	23.4	0.3
K _{β}	69.7	0.55

Table 3.1: X-ray satellite energies and intensities relative to the Al K _{α 1/2} line [37].

¹For this entire section the books of Hofmann [18] and Briggs and Seah [9] have been used as reference.

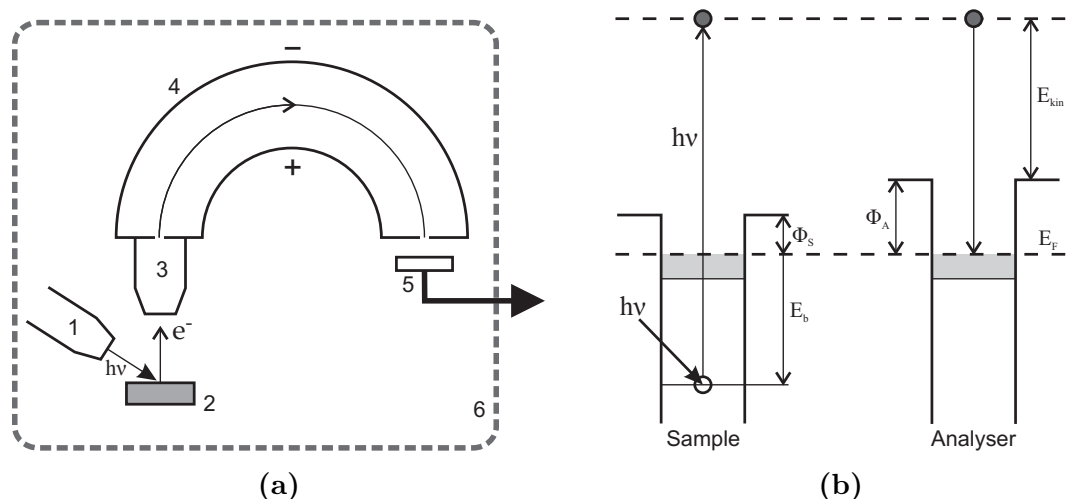


Fig. 3.1: Principle of XPS. (a) Instrumental components: 1) X-ray source, 2) sample, 3) electron lens, 4) hemispherical analyser, 5) detector, 6) vacuum enclosure. (b) Energy diagram of the XPS process.

Many lab systems utilise X-ray tubes as radiation source, equipped with Mg or Al anodes generating Mg K_α ($h\nu = 1253.6$ eV) or Al K_α ($h\nu = 1486.6$ eV) radiation, respectively. These sources are not monochromatic, but show a range of X-ray lines of various energies with different intensities. The acquired XPS spectrum therefore shows multiple peaks beside the expected peaks from the main X-ray line. As energies and relative intensities of the characteristic lines in the X-ray spectrum are well known (e.g. the minor Al K_α lines are shown in Tab. 3.1), those satellite peaks are fairly easy to account for in XPS analysis.

A different X-ray source for XPS measurements is synchrotron radiation, which allows for more complex experiments, as it has several advantages over conventional lab sources. Due to its high brightness, synchrotron radiation can be used to generate monochromatic X-rays for XPS with high energy resolution. Furthermore, the excitation energy $h\nu$ can be seamlessly tuned from a few hundred eV up to several keV. The term HAXPES (Hard X-ray Photoelectron Spectroscopy) refers to XPS experiments with excitation energies typically above 2 keV.

3.1.1 Qualitative Analysis of Photoelectron Spectra

In a photoelectron spectrum acquired by XPS, photoelectrons either originate from the valance band of solids, creating the valence band spectrum on the lower binding energy side up to approximately 20 eV [9], or from core levels of the atomic electron shells. The latter give rise to the main features in XPS, the photoelectron peaks. Their position in the spectrum directly corresponds to the element specific binding energies of the atomic core levels (equation (3.1)), giving information about the chemical elements that are present in a sample. These peaks are therefore correspondingly denoted by element and subshell (e.g. O 1s, Fe 2s, Fe 2p, Sr 3d).

Due to spin-orbit coupling, the subshells with angular momentum higher than s split up into two discrete energy levels, showing up as doublet peak structures in the photoelectron spectrum. Although the energy difference between both peaks depends on element and subshell, the intensity ratio is always the same (i.e. 1:2 for p, 2:3 for d, and 3:4 for f subshells [18]). Another effect that leads to multiple photoelectron peaks for a single core level is multiplet splitting. It occurs when an atom has unpaired electrons in its valence levels and a photoionization process leaves another unpaired electron in a core level behind. Depending on the electron spin, this core level electron can then couple with the valence level electrons, resulting in a number of different final states, affecting the binding energy of the emitted electron.

In compound materials, the bonding between different elements changes the binding energy of the core levels compared to the pure elemental state. In oxides for example, the oxygen atoms have higher electronegativity than the oxidized atoms, causing a static charge transfer of valence electrons towards the oxygen. This leads to a change of the effective atomic potential, resulting in different binding energies, depending on the oxidation state of the atom. The change in binding energy can be observed as a “chemical shift” in the photoelectron spectrum and thus the valence state of atoms can be determined (e.g. Fe^{2+} or Fe^{3+}).

Apart from the satellite peaks which result from non-monochromatic X-ray sources, as discussed in the beginning of this section, photoelectron peaks can be accompanied by a number of different satellite peaks on their high binding energy side of the spectrum. These are caused by interactions of the photoelectrons with other electrons during the photoemission process, resulting in discrete losses of kinetic energy. Shake-up satellites are caused by excitation of valence electrons to higher, unfilled valence levels. Plasmon loss peaks result from the excitation of oscillations of the free electron gas. These collective electron oscillations have discrete, material dependent frequencies which are different for bulk and surface oscillations.

Finally, Auger peaks can be observed in photoelectron spectra. These are the result of a secondary process after an atom has been ionized in one of its core levels. An electron from a higher level can drop into the vacant state, but instead of emitting a photon, another electron from the atomic shell is emitted. The kinetic energy of this photoelectron only depends on the energy differences between the involved core levels, but not on the excitation energy of the X-ray source. Auger peaks, like normal photoelectron peaks, can also be accompanied by the satellite peaks described above.

3.1.2 Quantitative Analysis of Photoelectron Spectra

Although X-rays can penetrate deeply into solid matter, photoelectrons are very susceptible to inelastic scattering. The inelastic scattering creates extensive background towards the high binding energy side of photoelectron peaks (lower kinetic energy). For quantitative analysis, this background has to be subtracted from the spectrum. If the background is relatively small compared to the peak intensity, this can be done with a simple linear approach. However, most photoelectron peaks show a significant higher background on their higher binding energy side. Physically this can be explained such

that the electrons registered for a certain binding energy also include inelastically scattered electrons from lower binding energies (higher kinetic energy). If one assumes that the chance for inelastic scattering is approximately the same over the given energy range, the background below a certain kinetic energy should be proportional to the photoelectrons above that energy that were not inelastically scattered. One technique, that tries to account for this, is the background subtraction after Shirley [30]. The Shirley background is an iterative method to calculate the background of a peak, that stretches from $E_{B,\min}$ to $E_{B,\max}$. If the spectrum of intensities I is decomposed into N channels with $E_B(N) = E_{B,\min}$ and $E_B(0) = E_{B,\max}$, the background B in the n -th channel for the $(i + 1)$ -th iteration is

$$B_{i+1}(n) = I(N) + (I(0) - I(N)) \frac{\sum_{n'>n} (I(n') - B_i(n'))}{\sum_{n'>0} (I(n') - B_i(n'))}. \quad (3.2)$$

For this, a first approximation of the background has to be supplied and the borders $E_{B,\min}$ and $E_{B,\max}$ must be carefully chosen.

The inelastic mean free path (IMFP) describes the average distance a photoelectron can travel through solid matter without losing energy due to inelastic scattering. It mainly depends on the kinetic energy of the electrons, but also on sample structure and composition. There is experimental data on IMFPs, but only for a limited number of substances and kinetic energies. Thus, the predictive TPP-2M formula [33], which is part of the NIST Standard Reference Database 71 [28], is used to calculate IMFPs in the energy range of 50 to 2000 eV. Typically, the IMFP λ is of the order of only a few nm, which makes XPS a surface sensitive technique. The information depth ID is used as a measure of the sampling depth of XPS experiments and can be expressed as

$$\text{ID} = -\lambda \cos(\varphi) \ln(1 - (P/100\%)), \quad (3.3)$$

where P is a percentage of the total signal intensity and φ is the detection angle relative to the surface normal [27]. Typically, $\text{ID}(P = 95\%)$ is chosen, which describes the sample depth from which 95% of the photoelectrons originate. For emission normal to the surface, equation (3.3) yields $\text{ID}(P = 95\%) \simeq 3\lambda$.

Quantitative XPS analysis involves the determination of intensities of individual photoelectron peaks. The line shape of these peaks is the result of line broadening due to several processes. On the fundamental physical level, the uncertainty principle leads to a natural broadening determined by the lifetime of the core level vacancy created by the photoemission process, which can be described by a Lorentzian function. On the experimental level, the instrumental response of analyser and detector and the line width of the X-ray source introduce line broadening, that can often be described by Gaussian functions. Furthermore, atomic vibrations impose temperature dependent Gaussian broadening. For clearly separated peaks, intensity determination can simply be done by integration over the respective energy range. However, if multiple peaks overlap, they need to be decomposed to get the individual contributions. This can be done by fitting a model that describes the intensity distribution for the expected photoelectron peaks

to the experimental data. For the individual line shapes, a combination of Gaussian and Lorentzian functions is used for the above mentioned reasons.

To calculate the integrated intensity of a photoelectron peak, the straight-line approximation can be used, as Newberg et al. [24] have done. For a film of thickness t , the integrated intensity is given by

$$I_f = S \cdot \lambda' \cdot (1 - e^{-t/\lambda'}), \quad (3.4)$$

with $\lambda' = \lambda \cos(\varphi)$ as the effective IMFP at angle φ between surface normal and detector. The limit for infinite film thickness ($t \rightarrow \infty$) in equation (3.4) yields the intensity from bulk material

$$I_b = S \cdot \lambda'. \quad (3.5)$$

In multilayer systems, the intensity I_0 (i.e. I_f or I_b) coming from a layer that is covered by n layers, is, after Newberg et al. [24], attenuated in each layer according to the Beer-Lambert law, so that the measured intensity becomes

$$I = I_0 \prod_{i=1}^n e^{-t_i/\lambda'_i}. \quad (3.6)$$

The photoemission spectroscopy constant S in equations (3.4) and (3.5) is given by

$$S = \Phi(h\nu) \cdot D(E_{kin}) \cdot \sigma(h\nu) \cdot \beta(h\nu, \Psi) \cdot N, \quad (3.7)$$

with N being the number of atoms per unit volume. If the directions of incident X-ray beam and photoelectron emission are at the ‘‘magic angle’’, i.e. $\Psi = 57.4^\circ$ [18], as is the case in most lab systems, the asymmetry parameter β becomes unity and the element and subshell specific photoionisation cross-sections σ can be looked up in tabulated work, e.g. by Scofield [29]. For angular resolved XPS the work of Trzhaskovskaya et al. [34] supplies a method to determine the element and subshell specific values for σ and β .

In this work, the dependence on kinetic energy of the spectrometer efficiency D will be assumed negligible for the compared photoelectron peaks, so that both, the X-ray flux Φ and D cancel, when evaluating intensity ratios. Furthermore, for comparison of peak intensities, the normalised intensity

$$I' = I/\sigma\beta \quad (3.8)$$

will be used.

3.1.3 Identification of Growth Modes using XPS

Monitoring variations of peak intensities in photoelectron spectra over the course of thin film growth, using successive XPS measurements, makes it possible to identify the growth mode of thin films. Assuming that $\lambda_s \simeq \lambda_f = \lambda$, which is true for photoelectrons with similar kinetic energy, the combination of equations (3.4) to (3.6) yields for idealised

layer-by-layer growth, that the relative intensity of a film peak f compared to a substrate peak s should increase with film thickness t as

$$Y = \frac{I'_f}{I'_f + I'_s \cdot \frac{N_f}{N_s}} = 1 - e^{-t/\lambda}. \quad (3.9)$$

Since coverages of fractional monolayers are realised by a partially covered surface, the intensity ratio (3.9) between coverages of integral monolayers is made up of linear segments, as Fig. 3.2a shows [25]. For idealised island growth, Oura et al. [25] describe the expected behaviour of the intensity ratio as linear with the substrate coverage (Fig. 3.2c). For layer plus island growth, the intensity ratio first follows that of layer-by-layer growth, but after the initial layer has formed and islands start to grow, it switches to that of island growth (Fig. 3.2b).

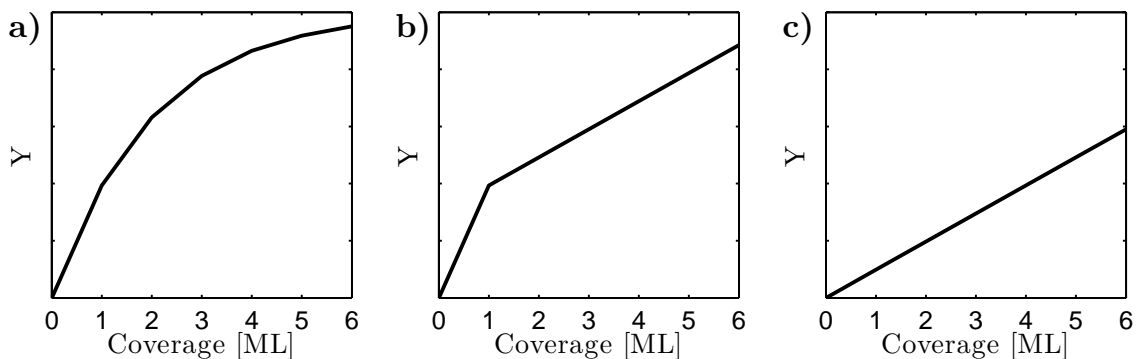


Fig. 3.2: Theoretically expected behaviour of the XPS peak intensity ratio (3.9) for (a) layer-by-layer growth, (b) layer plus island growth, and (c) island growth. After Oura et al. [25].

3.2 Low Energy Electron Diffraction²

Low energy electron diffraction (LEED) is a common technique used to characterise surface structures of crystalline materials. Electrons with low kinetic energy (30 to 200 eV), having wavelength in the order of atomic spacings (~ 1 to 2 \AA), can be elastically scattered by a crystal. An incident electron beam with wave vector \mathbf{k}_0 , elastically scattered by a crystal, produces diffracted beams with wave vector \mathbf{k} . From the spacial distribution of the diffracted beams, information about the crystal lattice can be gained, while the intensity of the diffracted beam gives information on the atomic arrangement within a unit cell. Because the scattering is elastic, conservation of energy

$$|\mathbf{k}| = |\mathbf{k}_0| \quad (3.10)$$

and conservation of momentum

$$\mathbf{k} - \mathbf{k}_0 = \mathbf{G}_{hkl} \quad (3.11)$$

²For this section the book of Oura et al. [25] has been used as reference.

can be used to describe the scattering process. With the reciprocal lattice vector \mathbf{G}_{hkl} , the diffraction pattern is directly related to the crystal reciprocal lattice. As the mean free path of electrons with low kinetic energy is very short, most elastic interaction of the electrons happen in the topmost atomic layers of the crystal. Because of that, LEED can be considered as diffraction on a 2D surface, where the Bragg points along the normal direction become infinitely dense spaced, resulting in reciprocal lattice rods, with equation (3.11) becoming

$$\mathbf{k}^{\parallel} - \mathbf{k}_0^{\parallel} = \mathbf{G}_{hk}. \quad (3.12)$$

For graphical representation of the scattering process, the Ewald construction, as shown exemplary in Fig. 3.3b, is used. It shows the lattice rods on a crystalline surface in the reciprocal space. The incident wave vector \mathbf{k}_0 is drawn so that it terminates on the (00) lattice rod at the sample surface. Centred at its origin, a circle with radius k_0 is constructed, representing the Ewald sphere. All interceptions of this circle with the lattice rods mark possible reflex spots, as there equations (3.10) and (3.12) are fulfilled. Fig. 3.3b also shows the numbering of reflex spots for a cubic lattice.

From the sharpness of the reflex spots and from their contrast against the background, conclusions on the crystallographic quality can be made. Random structural defects, crystallographic imperfections and small domain sizes result in broadening and weakening of reflex spots and an increase in background intensity, as the periodicity is reduced. The absence of any reflex spots indicates a disordered, amorphous, or finely polycrystalline surface.

The basic experimental setup of a LEED system is schematically shown in Fig. 3.3a. An electron gun, positioned over the centre of the sample, produces a beam with normal incidence on the sample surface. The diffracted electron beams are detected on a fluorescence screen and the image is captured by a CCD-camera through the viewport. It is apparent that, with a correctly positioned sample, the (00) reflex can not be seen in this geometry, as it is always located at the centre of the screen, where it is concealed by the electron gun.

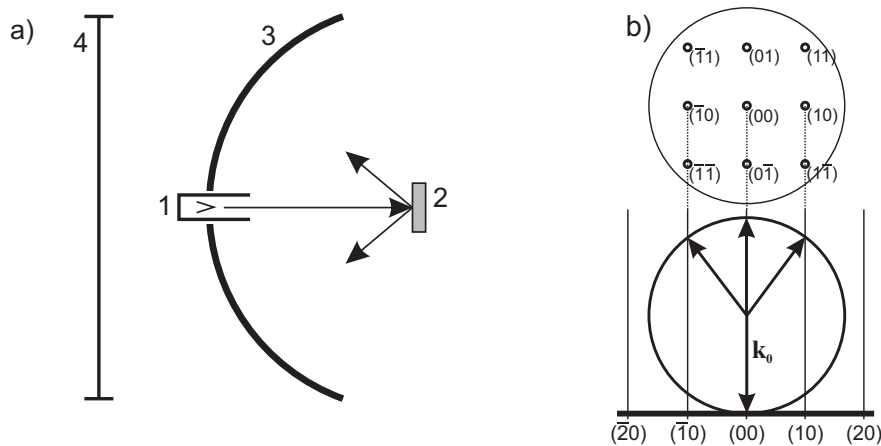


Fig. 3.3: (a) Basic experimental setup for LEED: 1) electron gun, 2) sample, 3) fluorescence screen, and 4) viewport. (b) Ewald construction for LEED (bottom) and labeling of LEED spots (top).

3.2.1 Facets

Samples with plain surface structures show LEED patterns as described above, with the (00) reflex always located at the centre of the screen. The position of all other reflex spots depends on the electron energy. With higher energies, the Ewald sphere gets larger, possibly encompassing more lattice rods, and in the projection on the screen the reflex spots therefore move inwards, towards the (00) reflex. If there are facets on the sample surface, e.g. islands with regularly oriented faces, inclined by an angle α , additional reflex spots can be detected in LEED.

Fig. 3.4 shows the Ewald construction for such a surface. An additional surface plane from the facets, inclined by the angle α , with corresponding lattice rods is superimposed to that of the plain surface. Its (00) reflex is not located at the centre of the LEED screen, but well outside, depending on electron energy and angle α . With increasing electron energy, the other reflex spots of that plane will also move towards their (00) reflex, which is towards the outside of the fluorescence screen, in opposite direction of the normal reflex spots.

The Ewald construction in Fig. 3.4 shows how this can be used to determine the inclination angle α of the facets. Two electron energies, E_1 and E_2 (wave vectors \mathbf{k}_1 and \mathbf{k}_2) have to be identified, where a reflex spot of a facet coincides with two different reflex spots of the plain surface. At these energies, lattice rods of the two surfaces intercept in the reciprocal space. With the reciprocal lattice vector $\mathbf{a}_0^* = 2\pi/\mathbf{a}_0$, the facet angle α can be calculated from the relation

$$\tan \alpha = \frac{a_0^*}{h_2 - h_1} = \frac{a_0^*}{(k_2 + \sqrt{k_2^2 - 4a_0^{*2}}) - (k_1 + \sqrt{k_1^2 - a_0^{*2}})}. \quad (3.13)$$

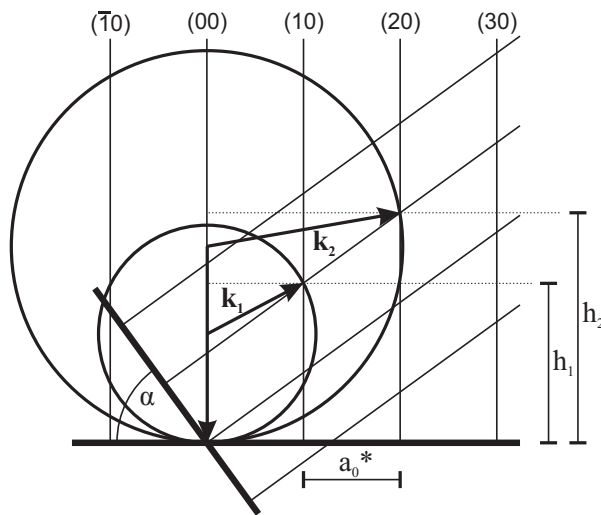


Fig. 3.4: Ewald construction for diffraction on a 2D surface with facets.

4 Materials and Sample Preparations

As thin film growth is very sensitive to surface contaminations, sample preparation is done under high vacuum conditions, i.e. in a vacuum chamber with a base pressure of less than 10^{-7} mbar, to avoid surface contamination by adsorption of atmospheric particles. Commercially available, ready to use single crystals are used as substrates. After being loaded into the vacuum system, they are annealed to remove all surface contaminations. The growth of thin metal oxide films on the clean substrate surface is then done using the technique of reactive molecular beam epitaxy (reactive MBE). An exemplary setup of a vacuum system for reactive MBE is schematically pictured with detailed descriptions in Fig. 4.1. Like normal MBE, a beam of metal atoms is generated by an evaporator and directed onto the sample. The impinging metal atoms are adsorbed on the sample surface, as are oxygen atoms from an O_2 atmosphere. Both, oxygen and metal atoms react on the sample surface, forming the metal oxide thin film. The stoichiometry of the metal oxide film is controlled by specifically adjusting the pressure of the O_2 atmosphere to the evaporator flux.

The evaporator consists of a metal rod which is heated using electron bombardment, by applying a high voltage of 1 to 1.3 kV between the metal rod and a heating element. As metal atoms from the rod sublimate, they are focused into a beam directed onto the sample surface by a hole in the surrounding evaporator casing. A shutter is used to

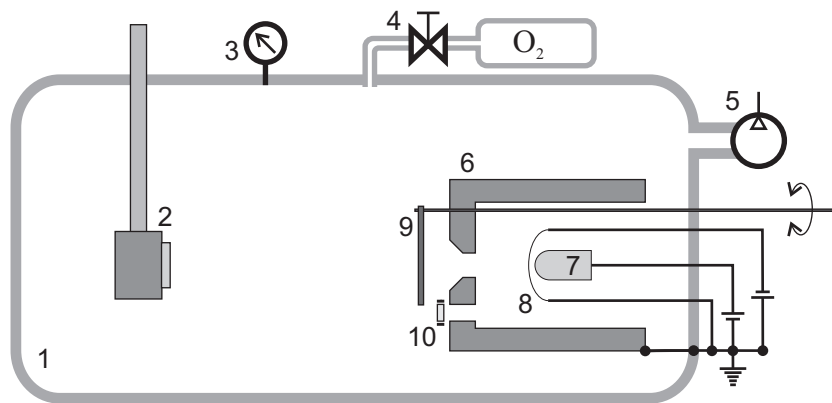


Fig. 4.1: Schematic representation of a vacuum system for thin film growth by reactive MBE: 1) vacuum chamber, 2) sample on sample holder with heating element and thermo couple, 3) vacuum gauge, 4) oxygen inlet with leek valve, 5) vacuum pump, 6) evaporator with: 7) metal rod, 8) heating element, 9) shutter, 10) crystal oscillator.

nearly instantly turn the beam on and off. The evaporator flux can be monitored by the frequency change of a crystal oscillator (quartz balance), whose frequency is detuned by deposited material. A leak valve in combination with a vacuum gauge is used to control the oxygen pressure in order to create a metal oxide with the desired stoichiometry. The sample is mounted on a heater block faced towards the evaporator. The sample temperature is monitored using a thermo-couple attached to the heater block.

4.1 Strontium Titanate

Strontium titanate, SrTiO_3 (STO), is an optically transparent, paraelectric insulator with an indirect bandgap of $E_g = 3.25$ eV [35]. It crystallises in the cubic perovskite structure with a lattice parameter of $a_0 = 3.901$ Å and one formula unit per unit cell [1]. The atomic structure of the bulk unit cell, given in Fig. 4.2, has strontium atoms at the cube corner positions, titanium at the body centre position and oxygen at the face centre positions. This leads to alternating TiO_2 and SrO layers in the $[001]$ direction and corresponding surface terminations of the (001) face are possible.

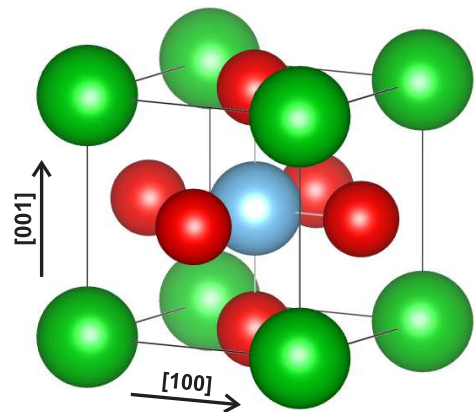


Fig. 4.2: Bulk unit cell of SrTiO_3 : Sr^{2+} in green, Ti^{4+} in blue, and O^{2-} in red.

In order to avoid charging of samples in XPS and LEED experiments, the STO single crystals used in this work are doped with small amounts of Nb, making them electrically conductive.

4.2 Magnetite¹

Magnetite, Fe_3O_4 , is a ferrimagnetic semiconductor with a Curie temperature $T_C = 850$ K and a bandgap $E_g = 0.1$ eV. It crystallises in the inverse spinel structure, a face centred cubic lattice with 8 formula units per unit cell, based on regularly cubic close packed oxygen O^{2-} anions in the $[111]$ direction. Stoichiometric magnetite has a lattice parameter of $a_0 = 8.396$ Å and a cation ratio of $\text{Fe}^{2+}/\text{Fe}^{3+} = 0.5$. The iron atoms are placed in the interstices of the anion structure with tetrahedral sites evenly occupied by divalent and trivalent iron, while the remaining trivalent iron occupies octahedral sites. The cubic unit cell of magnetite is shown in Fig. 4.3b. Its (001) face displays a (1×1) surface unit cell that is rotated by 45° and has a lattice parameter that is smaller by a factor of $1/\sqrt{2}$ compared to the bulk unit cell. Magnetite shows, in contrast to other iron oxides, a $(\sqrt{2} \times \sqrt{2})R45$ superstructure from a surface reconstruction of the (001)

¹Information on iron oxides is taken from the book of Cornell and Schwertmann [12].

surface, which gives it a distinctive LEED pattern [10]. One monolayer of magnetite is defined by Voogt et al. [36] as 0.21 nm, i.e. 1/4 the height of the unit cell.

Thin film growth of magnetite is very sensitive to process parameters, as the other iron oxides wüstite and maghemite are closely related in that they are both also based on regularly cubic close packed oxygen anions. Wüstite, FeO, has no stable stoichiometric phase and is thus written as Fe_{1-x}O , having most of its iron atoms in the divalent state. Maghemite, $\gamma\text{-Fe}_2\text{O}_3$, on the other hand, has most of its iron atoms in the trivalent state. As mentioned in section 3.1.1, the valance state of atoms in a material can be identified by the chemical shift of photoelectron peaks in the XPS spectrum. For the iron oxides, the valance state of iron can be identified by the position of a characteristic satellite between the Fe $2p_{1/2}$ and Fe $2p_{3/2}$ doublet peaks (Fig. 4.3a) [16, 40]. Divalent iron shows a distinctive satellite peak on the foot of the Fe $2p_{3/2}$ peak, while trivalent iron shows a distinctive satellite peak on the foot of the Fe $2p_{1/2}$ peak. For stoichiometric magnetite no satellite peak is visible between the Fe 2p doublet peak.

The divalent iron in magnetite can be replaced by other divalent ions [12]. For example, replacing the Fe^{2+} ions with Ni^{2+} ions yields nickel ferrite (NiFe_2O_4 , NFO).

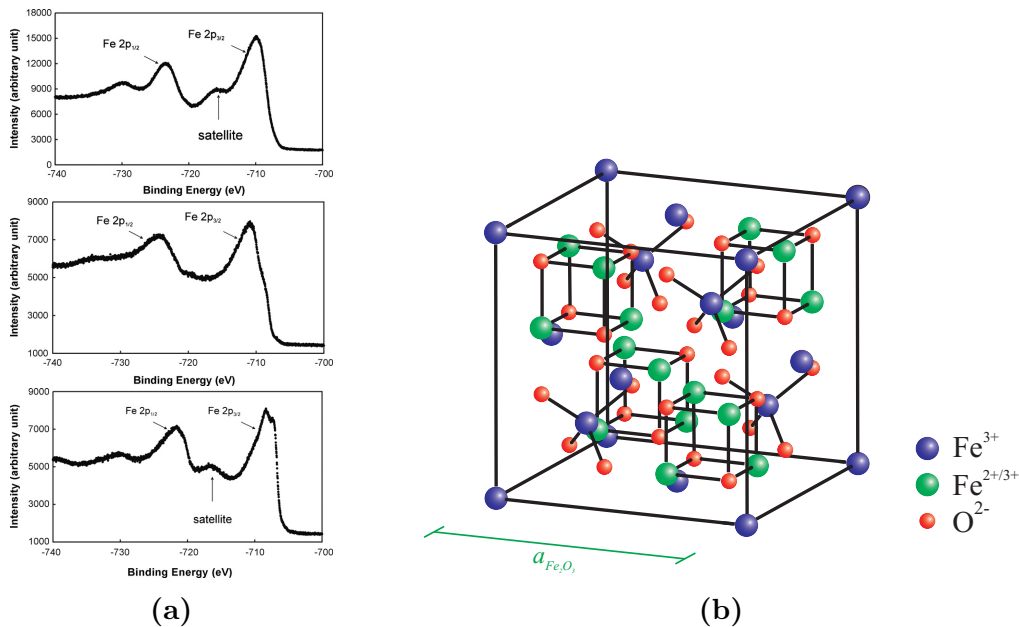


Fig. 4.3: (a) XPS reference spectra of the iron oxides (from top to bottom): Fe_{1-x}O , Fe_3O_4 , and Fe_2O_3 . Images taken from Yamashita and Hayes [40]. (b) Bulk unit cell of Fe_3O_4 (image taken from the work of Bertram [4]).

4.3 Nickel Oxide

Nickel oxide, NiO, is an antiferromagnetic insulator with a bandgap of $E_g = 4.2$ eV. It crystallises in the rock salt structure, as is shown in Fig. 4.4, with a lattice parameter of $a_0 = 4.17$ Å and 4 formula units per unit cell [13]. Compared to the bulk unit cell, the surface unit cell of the (001) face of NiO is rotated by 45° and its lattice parameter is smaller by a factor of $1/\sqrt{2}$.

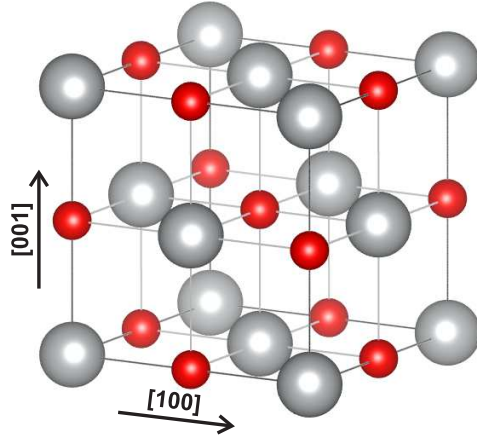


Fig. 4.4: Bulk unit cell of NiO: Ni²⁺ in grey, and O²⁻ in red.

5 Growth of Ultrathin Fe₃O₄ Films on STO Support

In this part the growth process of ultrathin Fe₃O₄ films on STO(001) substrates is studied. Although the surface energies of the STO(001) surface ($\gamma_{\text{SrTiO}_3(001)} = 1.0 \text{ J m}^{-2}$) and the Fe₃O₄(001) surface ($\gamma_{\text{Fe}_3\text{O}_4(001)} = 1.4 \text{ J m}^{-2}$) [31] clearly suggest island growth according to equation (2.4), smooth epitaxial magnetite layers are sought-after for technical applications. This study tries to identify growth parameters to match this demand.

5.1 Experimental Setup

Four samples have been created to investigate the influence of different parameters on the growth mode of ultrathin Fe₃O₄ films. Sample preparation has been conducted as described in chapter 4. The STO substrates, SrTiO₃ single crystals with 0.05 wt. % Nb, have been supplied by SurfaceNet GmbH. They are (001) oriented and $10 \times 10 \times 0.5 \text{ mm}^3$ in size, with a polished surface. Annealing of the substrates has been done at 400 °C for one hour in an oxygen atmosphere of 1×10^{-4} mbar. On these clean substrates Fe₃O₄ films have been grown in several small steps, using reactive MBE as described in chapter 4. Two of the samples have been heated to 250 °C for deposition, the other two to 450 °C. On each of the samples with different temperature, iron has been deposited at two different deposition rates, with the oxygen pressure chosen so that magnetite forms on the samples. Tab. 5.1 gives an overview of the process parameters for the four samples.

Deposition steps of only a few monolayers have been made at first, as to closely monitor the initial growth phase. Later, steps have been chosen wider, as the observed changes have become smaller. In total, between nine and eleven deposition steps have been made on each sample over the course of two to four days, without breaking UHV conditions. After every deposition step, XPS and LEED measurements have been made.

	Slow250	Slow450	Fast250	Fast450
T_{sample}	250 °C	450 °C	250 °C	450 °C
$p(\text{O}_2)$	5×10^{-7} mbar	5×10^{-7} mbar	9×10^{-7} mbar	9×10^{-7} mbar
$\Delta f_{\text{quartz balance}}$	15.6 kHz	24.5 kHz	13.3 kHz	34.8 kHz
deposition rate	4.18 nm/h	4.08 nm/h	45.4 nm/h	38.97 nm/h
film thickness t_{XRR}	(12.3 ± 1.3) nm	(21.1 ± 2.2) nm	(12.7 ± 1.3) nm	—
total coverage	(59 ± 6) ML	(100 ± 10) ML	(61 ± 7) ML	(143 ± 29) ML

Table 5.1: Parameters for thin film growth of Fe₃O₄ on the four samples.

5.2 Determination of Film Thickness and Stoichiometry

As has already been mentioned, there are two closely related iron oxide species that can form instead of magnetite, if the oxygen pressure does not match the iron flux in reactive MBE. To verify that in each deposition step magnetite has formed, the Fe 2p spectrum of the XPS measurements (Fig. 5.2) is analysed after every deposition step, as described in section 4.2. No satellite peak between the Fe 2p_{1/2} and Fe 2p_{3/2} peak seems to be visible, indicating that throughout the complete deposition process stoichiometric magnetite has formed on all samples.

The amount of material deposited on the samples, i.e. the coverage, is assumed to be equal to the film thickness determined by XRR measurements. The X-ray reflectivity of a thin film shows intensity oscillations, also known as Kiessig fringes, due to phase differences between the beams directly reflected at the film surface and the refracted beam, that is reflected at the interface to the next deeper layer. For a single film on a substrate, the Kiessig fringes only show a single oscillation and the film thickness

$$t = \frac{m\lambda}{2\sqrt{\Theta_m^2 - \Theta_c^2}} \quad (5.1)$$

can easily be determined from the critical angle Θ_c and the position Θ_m of the m -th oscillations maximum [8].

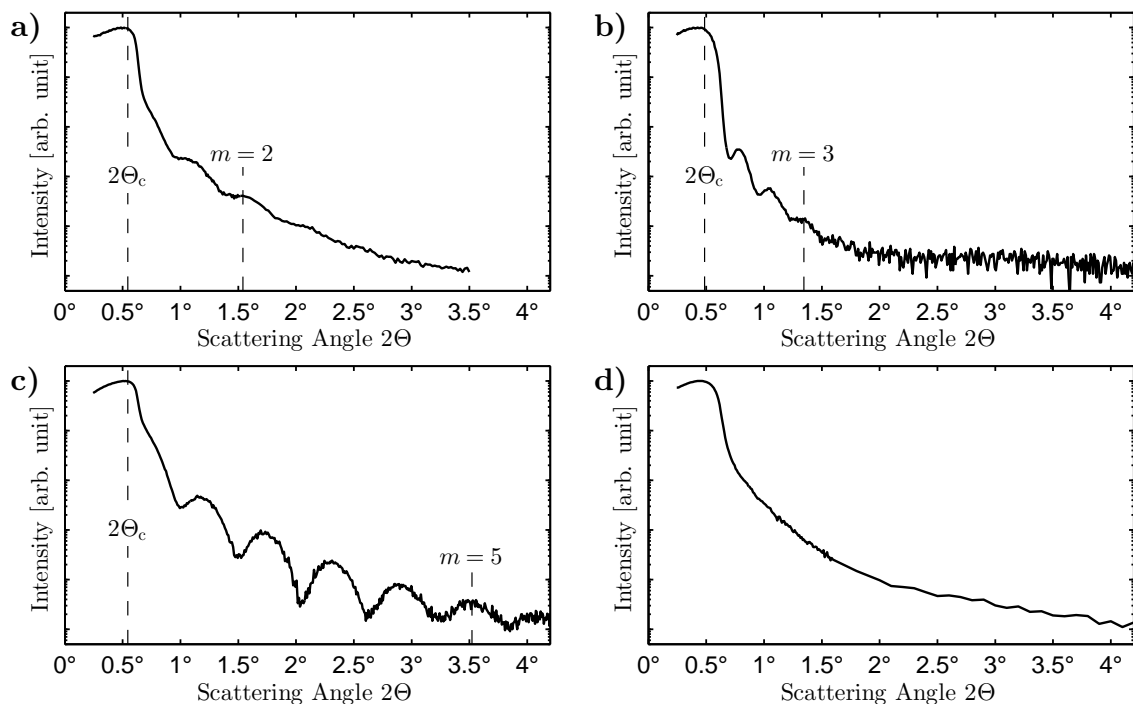


Fig. 5.1: XRR data from samples (a) Slow250, (b) Slow450, (c) Fast250, and (d) Fast450.

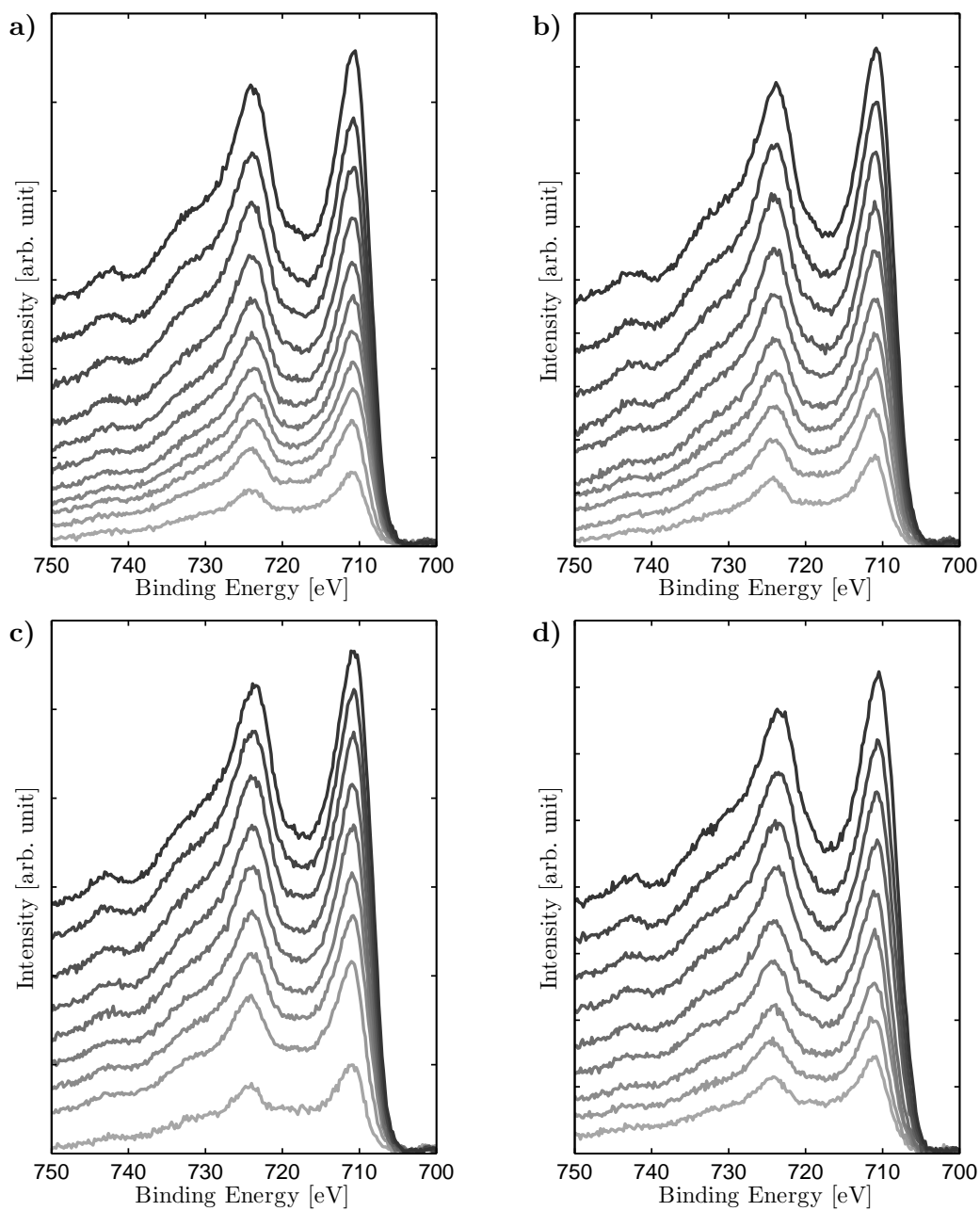


Fig. 5.2: Fe 2p photoelectron spectra of successive deposition steps (from bottom to top) for samples (a) Slow250, (b) Slow450, (c) Fast250, and (d) Fast450.

The XRR data from all but sample Fast450, shown in Fig. 5.1, display intensity oscillations from a single film, so that their thickness's can be determined after equation (5.1) and the results are presented in Tab. 5.1. As sample Fast450 shows no fringes in its XRR data, supposedly due to a very rough surface, its coverage is determined from the total frequency change of the quartz balance, compared to that for sample Slow450. This is believed to be a fairly good estimation, as the comparison of the quartz balance data to the XRR data for the other three samples yields quite good agreement. Sample Fast450 has been chosen for reference, because of the same deposition temperature. The coverage after the individual deposition steps on each sample is calculated from the final coverage, weighted by the time the shutter has been open in each step, as this is believed to be more accurate than the quartz balance.

5.3 Determination of Growth Modes

The investigation of the growth mode of the thin Fe₃O₄ films is, first of all, done by comparison of photoelectron intensities from XPS measurements, as described in section 3.1.3. The intensities of the substrate Ti 3p peak and the film Fe 3p peak have been chosen for this, because they are positioned closely together on the high kinetic energy side of the spectrum, so that the relative difference in kinetic energy is very small and thus their IMFPs ($\lambda_{\text{Fe } 3p} = 2.62 \text{ nm}$ and $\lambda_{\text{Ti } 3p} = 2.64 \text{ nm}$) can be seen as nearly identical. This is the necessary assumption for equation (3.9), which is used to identify the growth mode.

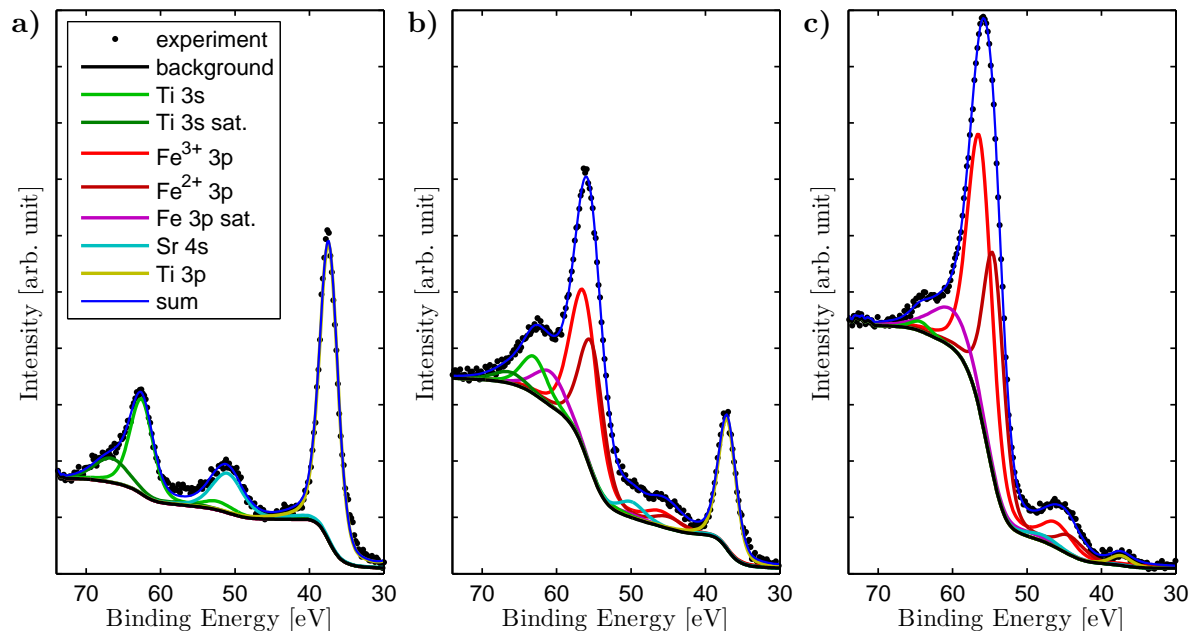


Fig. 5.3: Fe 3p photoelectron spectra of sample Fast250 after different deposition steps: (a) before deposition, (b) after five deposition steps (12.4 ML Fe₃O₄), and (c) after nine deposition steps (60.5 ML Fe₃O₄). Different lines show the functions used to fit the various peaks in the spectra.

One problem that arises is, that the Fe 3p film peak is partially superimposed by other peaks, as can be seen in Fig. 5.3. To solve this, a model describing all peaks suspected in the spectrum is derived and fitting it to the experimental data is used to determine peak intensities. After subtracting a Shirley background, the spectrum is decomposed into the peaks mentioned in Fig. 5.3a. The Fe 3p peak is made up of two peaks, one for divalent iron and one for trivalent iron. Furthermore, both, the Fe 3p and the Ti 3s peak are accompanied by a satellite peak on their high binding energy side. The relative intensity of these peaks has been kept fixed. Satellite peaks on the low binding energy sides result from minor X-ray lines due to the non-monochromatic X-ray source used and are modelled with a fixed ratio to their main peak, according to Tab. 3.1. For the lineshape of the individual peaks, the sum of a Gaussian and a Lorentzian function with the ratio 60:40 is used. Finally, the film intensity is made up of the sum of the two Fe 3p peaks and the Fe 3p satellite peak.

The intensity ratio according to equation (3.9), giving information on the thin film growth mode, is shown in Fig. 5.4 for all four samples, together with the curve for ideal layer-by-layer growth from equation (3.9). For the 250 °C samples, the curves show a similar behaviour compared to ideal layer-by-layer growth, but with a smaller slope. This can be explained, such that nucleation of a new layer starts before the growth of the last layers has finished, so that small islands exist on top of a stack of mostly completed layers. The film grown with a faster deposition rate is closer to ideal layer-by-layer growth than is the film grown with a slower deposition rate, although for the first six monolayers there is no difference between the two samples. The films deposited at a sample temperature of 450 °C resemble more to layer plus island growth, as for the first 3 to 5 monolayers the curves follow those of the 250 °C samples, but then the slope drastically decreases. Between those two samples there is little difference in the growth mode within the margin of error.

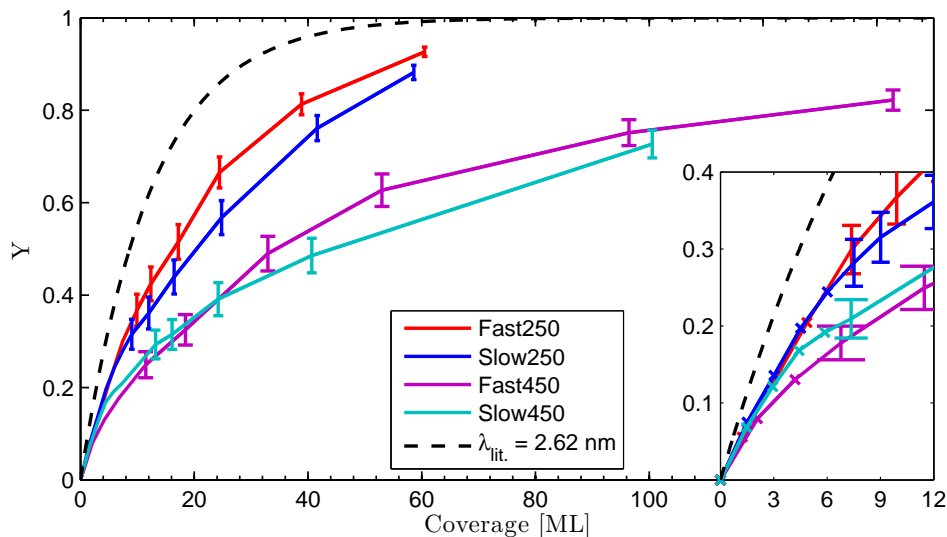


Fig. 5.4: Intensity ratios of the Fe 3p and Ti 3p peak according to (3.9) at different coverages of the four samples, and curve for ideal layer-by-layer growth. Error bars for the first steps are omitted for clarity.

AFM images of the final films (Fig. 5.5), measured ex-situ at the physics department of Bielefeld University¹, confirm these findings. Results from the evaluation of the AFM images are given in Tab. 5.2. The RMS roughness and the mean island height are calculated by the program of Horcas et al. [19]. The average distance between islands is obtained from line scans across the entire image, averaging over several directions. Exemplary line scans for the four samples are also shown in Fig. 5.5. The films deposited at 250 °C sample temperature show much smaller islands with average heights between 3 to 4 nm compared to the films deposited at 450 °C sample temperature, which show very tall islands with average heights between 7 to 8 nm. Also the density of islands is much higher on the 250 °C samples with average distances between islands only about half as wide. The deposition rate has an influence on the number of islands on the surface. Although the RMS roughness and the mean island height do not change very much for the two deposition rates, the distance between islands is, for the faster deposition

¹Thanks to Alexander Böhnke.

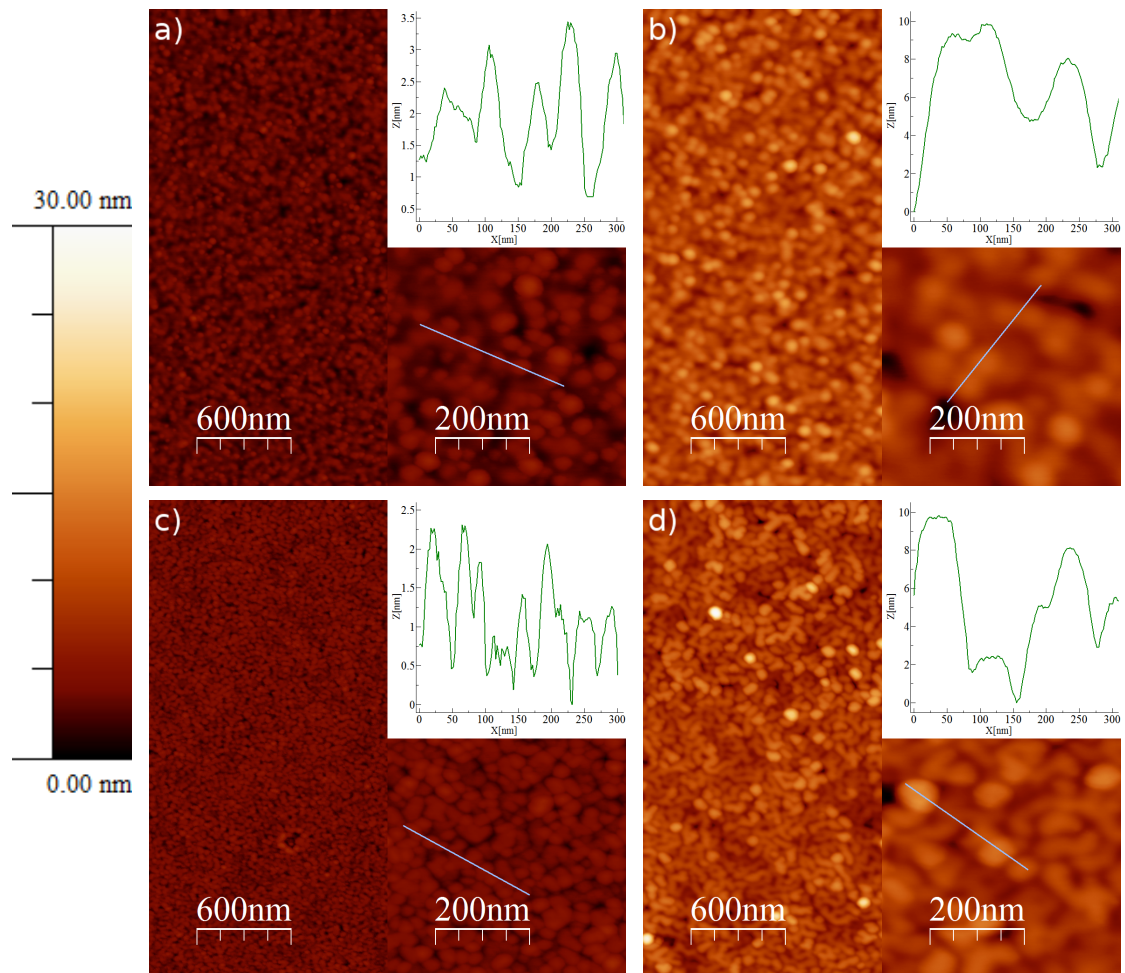


Fig. 5.5: AFM images at different resolutions and line-scans of samples (a) Slow250, (b) Slow450, (c) Fast250, and (d) Fast450.

rate, much smaller, which correlates to a higher island density, that can be clearly seen comparing the AFM images of the 250 °C samples.

	Slow250	Slow450	Fast250	Fast450
RMS roughness	0.95 nm	2.06 nm	0.78 nm	2.37 nm
mean island height	3.2 nm	7.2 nm	3.7 nm	8.3 nm
mean island spacing	61 nm	118 nm	38 nm	82 nm

Table 5.2: Evaluation of the AFM data (Fig. 5.5).

5.4 Determination of Film Structures

From the LEED images acquired after each deposition step, it is tried to reconstruct the structural order of the film during the growth process. Especially the initial phase of the supposedly epitaxial growth is of interest. There are five different structures, that can be observed in the LEED images. First, there is the (001) oriented STO substrate, that shows very sharp reflex spots for its (1×1) 2D surface lattice (Fig. 5.6a). The Magnetite (001) surface shows also a (1×1) structure in LEED (Fig. 5.6c), that is smaller by a factor $1/\sqrt{2}$ and rotated by 45° compared to the STO(001) surface structure. It also shows a $(\sqrt{2} \times \sqrt{2})R45$ superstructure from its surface reconstruction. Rather unsuspected, reflex spots with a 12-fold symmetry (Fig. 5.6b) have been discovered after the first deposition steps. From the work of Leung et al. [22], who have studied epitaxial $\text{Fe}_3\text{O}_4(111)$ on $\text{STO}(001)$, this can be identified as the hexagonal surface lattice of the $\text{Fe}_3\text{O}_4(111)$ surface, that can grow in two, by 30° rotated orientations on $\text{STO}(001)$. The 12-fold symmetry is the result of the superposition of reflexes from domains with different orientations. At last, facets (chapter 3.2.1) can be observed in the LEED experiments from reflex spots moving along the four main directions of magnetite (001). For the $[010]$ direction, this is demonstrated in Fig. 5.7. With increasing energy, a reflex spot moves away from the (00) reflex towards the (20) reflex of the $\text{Fe}_3\text{O}_4(001)$ surface lattice. At

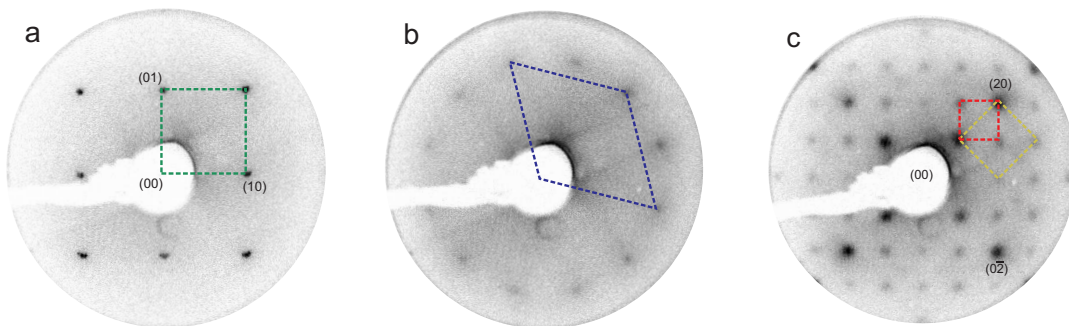


Fig. 5.6: Surface structures identified by LEED during thin film growth of Fe_3O_4 on STO: (a) (1×1) surface structure (green) of clean STO substrate, (b) 12-fold reflex symmetry of initial growth phase, and (c) (1×1) surface structure (yellow) of $\text{Fe}_3\text{O}_4(001)$ with $(\sqrt{2} \times \sqrt{2})R45$ superstructure (red).

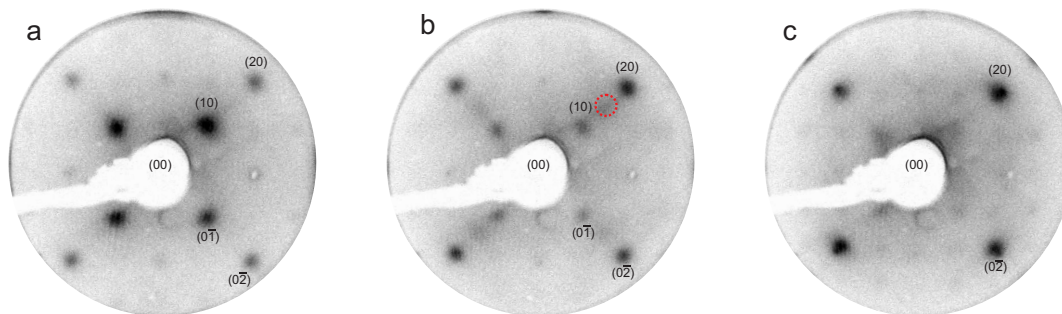


Fig. 5.7: LEED images of the same sample at different electron energies demonstrating facets along the [010] direction: (a) at 52 eV coinciding with the (10) reflex, (b) at 58 eV between the (10) and (20) reflex, and (c) at 70 eV coinciding with the (20) reflex.

an electron energy of 52 eV (Fig. 5.7a), the facet reflex coincides with the (10) reflex, at 58 eV (Fig. 5.7b) it is between the (10) and (20) reflex, and at 70 eV (Fig. 5.7c) it coincides with the (20) reflex. From these observations, equation (3.13) yields a facet angle of $54^\circ \pm 6^\circ$, which corresponds to the Fe₃O₄ [111] facet as described by Takahashi et al. [31], who gives a value for the facet angle of 54° . All facets observed in the LEED experiments show this orientation.

A thorough investigation of all LEED experiments for the above described features has resulted in the phase diagrams shown in Fig. 5.8 for all four samples. These indicate what surface structures have been observed after certain deposition steps and corresponding coverages. Between the two deposition rates, no significant differences can be observed in the LEED experiments. For the 250 °C samples, the LEED pattern of the substrate has already disappeared after the second deposition step, i.e. only after a few monolayers, indicating a mostly closed film on the surface. Then the 12-fold symmetry reflex spots of a Fe₃O₄(111) layer appear, that can be seen for up to a coverage of 30 to 50 monolayers. Facets appear shortly after the Fe₃O₄(111) layer, at a coverage of about 10 monolayers. As these indicate island growth, the Fe₃O₄(111) phase may be estimated to be no more than 10 monolayers thick, but can be seen much longer in LEED, as it gets not completely covered in the following deposition steps. The (1 × 1) Fe₃O₄(001) surface structure always appears after the facets at about 20 to 40 monolayers, but before the $(\sqrt{2} \times \sqrt{2})R45$ superstructure, that appears at a coverage of around 50 monolayers. For the 450 °C samples, the main difference is, that the substrate reflex spots are still visible after a coverage of 30 to 60 monolayers, indicating that there are massive holes from de-wetting in the film, confirming island growth.

5.5 Discussion

Summing up thin film growth of Fe₃O₄ on STO (001), there first appears an interface layer of (111) oriented Fe₃O₄, on which (001) oriented islands, with (111) faces start to grow. For the samples with deposition temperature of 250 °C, the analysis of the

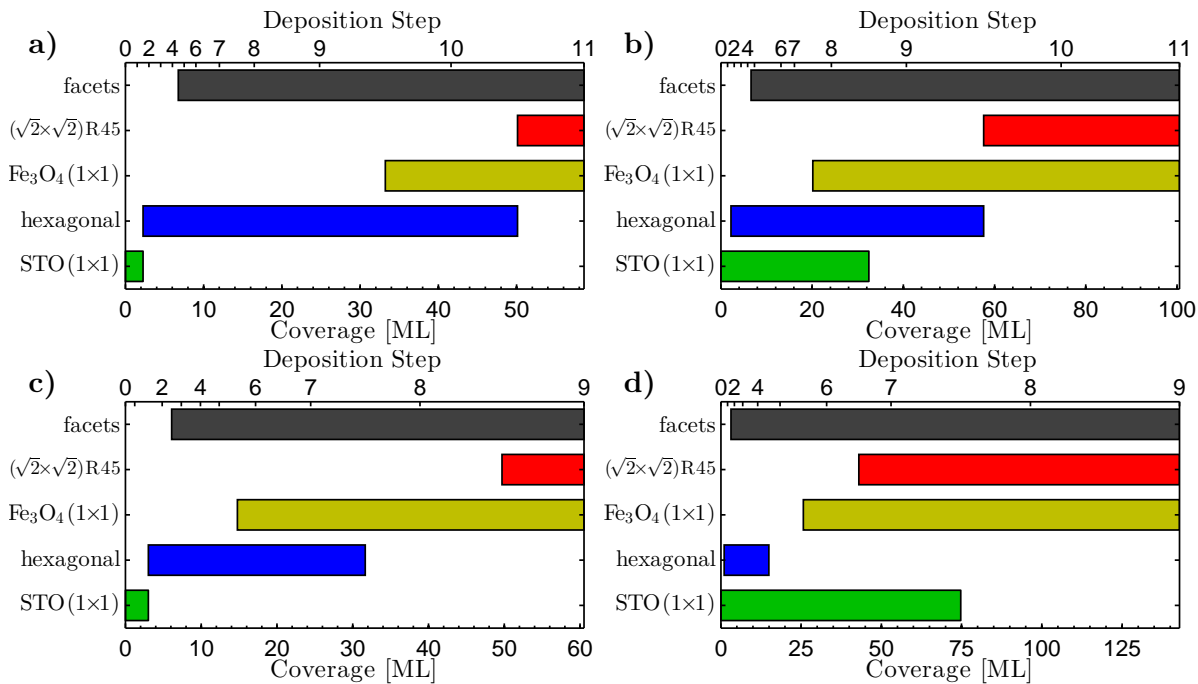


Fig. 5.8: Features in LEED images appearing at successive deposition steps on samples (a) Slow250, (b) Slow450, (c) Fast250, and (d) Fast450.

Fe 3p intensity ratios suggests a growth mode close to layer-by-layer growth, while for the samples with deposition temperature of 450 °C, it clearly indicates layer plus island growth. The size and density of these islands depends on sample temperature and deposition rate. The stepwise deposition of the Fe_3O_4 films seems to have no influence on the stoichiometry, as the evaluation of the Fe 2p spectra shows.

At higher sample temperatures, the nucleation rate of islands is believed to be small due to a very high surface diffusion rate, so that atoms on the surface can travel farther, before they are incorporated in already formed islands. This results in the growth of few, but big islands. On the other hand, at lower sample temperatures, the surface diffusion rate is much smaller, so that more, but smaller islands grow. As a higher deposition rate increases the nucleation rate, it further enhances the growth of many, densely spaced islands. With these, coalescence is more likely, resulting in closed film layers.

The observation of a Fe_3O_4 (111) oriented interface layer and the growth of islands with (111) oriented faces comes to the conclusion, that the surface energy for the Fe_3O_4 (111) surface has to be smaller than that of the (001) surface ($\gamma_{\text{Fe}_3\text{O}_4(001)} = 1.4 \text{ J m}^{-2}$). Reference data from Takahashi et al. [32] confirms this with a surface energy $\gamma_{\text{Fe}_3\text{O}_4(111)} = 0.22 \text{ J m}^{-2}$, that is even lower than that of the STO (001) surface ($\gamma_{\text{SrTiO}_3(001)} = 1.0 \text{ J m}^{-2}$) and explains the formation of the closed interface layer. However, no explanation could yet be found, as to why the growth of the initial (111) interface layer stops and (001) oriented islands start to grow on top. It is also unclear, what influence the interrupted growth process has, so that further experiments are necessary. One possibility to study the continuous growth of Fe_3O_4 on STO (001) may be RHEED experiments.

So far, these results suggest for the growth of Fe_3O_4 films on STO (001) a low sample

temperature and a high deposition rate. Maybe even higher deposition rates could yield better results for a layer-by-layer film structure with a smooth surface, but the experimental approach used in this study is at its limits, as the deposition steps become very short.

6 Interlayer Diffusion in Post Deposition Annealing

This part studies diffusion effects in $\text{Fe}_3\text{O}_4/\text{NiO}$ double layers on SrTiO_3 substrates from sample annealing after film growth. Two samples have been prepared with different interlayer thickness's and three annealing steps have been carried out on each at increasing temperatures. The main experiments have been conducted at beamline I09 of the Diamond Light Source.

6.1 Sample Preparation

Preparation of the samples has been done as described in chapter 4. The STO substrates, SrTiO_3 single crystals with 0.05 wt. % Nb, have been supplied by SurfaceNet GmbH. They are (100) orientated and $10 \times 10 \times 0.5 \text{ mm}^3$ in size, with a polished surface. Annealing of the substrates has been done at 400°C for one hour in an oxygen atmosphere of 1×10^{-4} mbar. LEED images of the annealed substrates are shown in Fig. 6.1a and Fig. 6.2a. Very sharp reflex spots from the (1×1) 2D lattice structure of the STO (001) surface can be seen with negligible background intensity. This indicates a clean surface with a long ranged structural order.

Deposition of the NiO layers has been done at a sample temperature of 250°C in an oxygen atmosphere of 1×10^{-5} mbar with a deposition rate of approximately 1 nm/min. The LEED image of the sample with a thin NiO layer is shown in Fig. 6.1b, that of the sample with a thick NiO layer is shown in Fig. 6.2b. Both show the (1×1) 2D

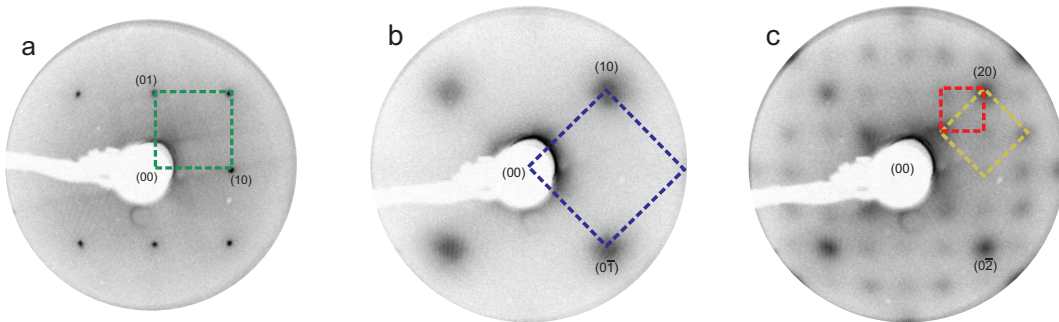


Fig. 6.1: LEED images of the sample with thin NiO interlayer at an electron energy of 74 eV: (a) STO substrate, (b) NiO layer, (c) Fe_3O_4 layer. Dashed squares indicate the (1×1) surface structures of STO (green), NiO (blue), and Fe_3O_4 (yellow). The $(\sqrt{2} \times \sqrt{2})\text{R}45$ superstructure of magnetite is indicated in red.

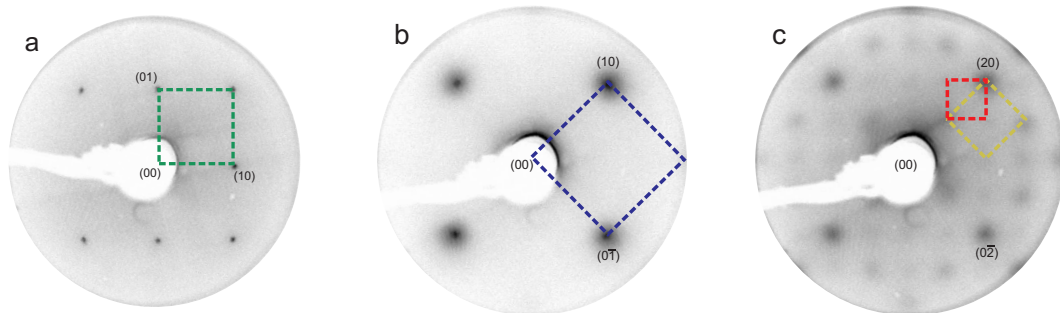


Fig. 6.2: LEED images of the sample with thick NiO interlayer at an electron energy of 74 eV: (a) STO substrate, (b) NiO layer, (c) Fe_3O_4 layer. Indications as explained in Fig. 6.1.

lattice structure of the NiO (001) surface, which is rotated by 45° compared to the STO surface lattice, as is mentioned in section 4.3, so that the bulk NiO lattice has the same crystal orientation as the STO substrate. The reflex spots of the thin layer are broader than those of the thick layer and their FWHM is greater by 27.5%, indicating a lesser crystallographic order. This may be caused by dislocations in the lattice structure, as the strain induced due to the high lattice misfit of 6.9% for NiO on STO, has not yet fully relaxed in the thin NiO layer. As no spots from substrate reflexes can be seen, supposedly closed layers are grown on both samples.

Fe_3O_4 layers grown on top of the NiO layers have a lattice misfit of 0.7% compared to bulk NiO. Deposition has been done at a sample temperature of 250°C in an oxygen atmosphere of 5×10^{-6} mbar with a rate of approximately 5 nm/min. LEED images for both samples (Fig. 6.1c and Fig. 6.2c) show the expected (1×1) 2D lattice structure, as well as the $(\sqrt{2} \times \sqrt{2})\text{R}45$ superstructure of the magnetite surface reconstruction, with the same growth orientation as the NiO layer.

XPS measurements made after every preparation step show no contamination and the growth of magnetite in the second layer can be confirmed by the shape of the Fe 2p spectra. The layer thickness's have been determined by the XRR measurements shown in Fig. 6.3. The experimental reflectivity data has been fitted using an XRR simulation program [3] and the resulting layer thickness's are given in Tab. 6.1.

Sample	NiO layer	Fe_3O_4 layer
thin NiO interlayer	1.5 nm	5.4 nm
thick NiO interlayer	5.6 nm	5.5 nm

Table 6.1: Layer thickness's determined from the XRR data in Fig. 6.3.

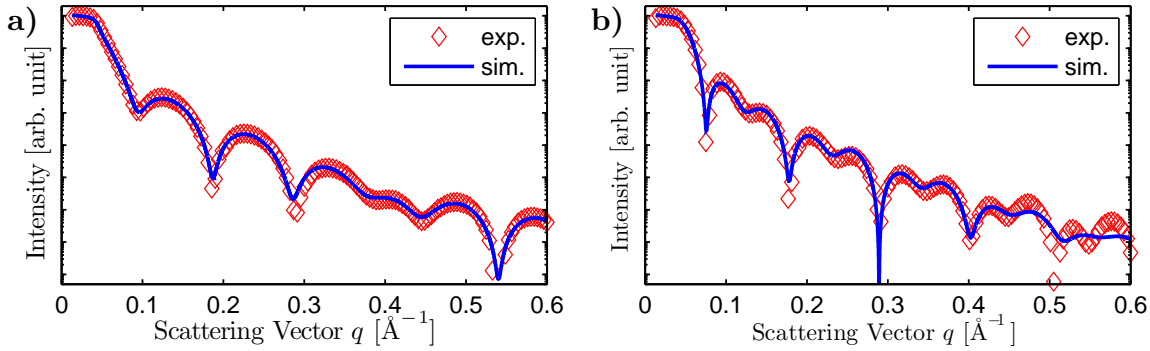


Fig. 6.3: XRR experimental and simulated data for (a) the sample with thin NiO interlayer and (b) the sample with thick NiO interlayer.

6.2 Experimental Setup

The studies on interdiffusion caused by sample annealing have been carried out under UHV conditions on Beamline I09 at the Diamond Light Source synchrotron. The samples have each been heated in three steps at different temperatures and XPS, HAXPES and LEED measurements have been made after every step. The heating has been done on a ceramic heater block in an oxygen atmosphere of 5×10^{-6} mbar and the temperature has been monitored using a thermo-couple and by checking the power of the heating element against reference data. The annealing steps have been: 20 minutes at 400 °C, 30 minutes at 600 °C, and 30 minutes at 800 °C.

Two types of XPS measurement have been carried out: A XPS survey with an excitation energy $h\nu = 1000$ eV, giving information with a surface near scope, and angular resolved HAXPES measurements with an excitation energy of 5934 eV, giving information with a range down to the substrate. The geometry for the angular resolved HAXPES measurement is pictured in Fig. 6.4. The X-ray beam strikes the sample at the angle Θ with respect to the plane surface and the emission angle φ of the photoelectrons is

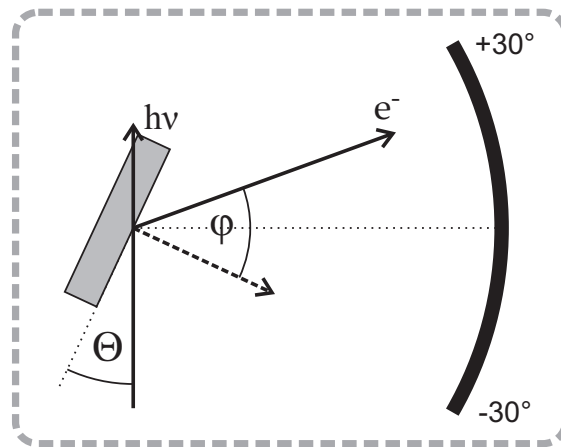


Fig. 6.4: Geometry for angular resolved HAXPES on Beamline I09 at Diamond Light Source: sample on the left and “detector” on the right.

measured relative to the surface normal of the sample. The 2D electron detector can be operated in an angular mode with an acceptance angle of nearly 60° , allowing for simultaneous acquisition of XPS data for different photoelectron emission angles.

For this study, the acceptance angle of the detector has been divided into seven slices, each covering approximately 7° of the acceptance angle. The sample with thin NiO interlayer has been measured each time at three different sample angles $\Theta = 11^\circ$, 25° , and 39° , spanning a total emission angle range of -10.5 to 58.5° , with an overlap of five slices between successive sample angles. This has been done to verify that the detector sensitivity is independent of the entrance angle of the photoelectrons. Due to time constraints, the sample with thick NiO interlayer has only been measured at $\Theta = 25^\circ$, giving a photoelectron emission angle range of 3.5 to 44.5° .

6.3 Surface Analysis

Using LEED images acquired after every annealing step, in conjunction with data from XPS measurements, structural changes and the crystalline quality near the sample surface are investigated.

Before the first annealing step, LEED images of the samples show very high background intensity and no reflex spots can be identified. As the samples have been exposed to normal atmosphere after fabrication, it is supposed, that an strongly disordered layer of molecules adsorbed from air has formed on top of the crystalline film. This is supported by the XPS measurement from before annealing of the sample with thick NiO interlayer (Fig. 6.7a), which shows a strong signal for the C 1s photoelectron peak. As carbon has not been present in the sample after the completion of sample preparation, it has to be part of a contamination layer.

After the first annealing step at 400°C the intensity of the C 1s peak has decreased, but the LEED images (Fig. 6.5a and Fig. 6.6a) still have very high background intensity, corresponding to a still highly disordered surface. After the 600°C annealing step all surface contaminations are removed from both samples according to the disappearance of the C 1s photoelectron peak in the XPS data of both samples (Fig. 6.7). The LEED

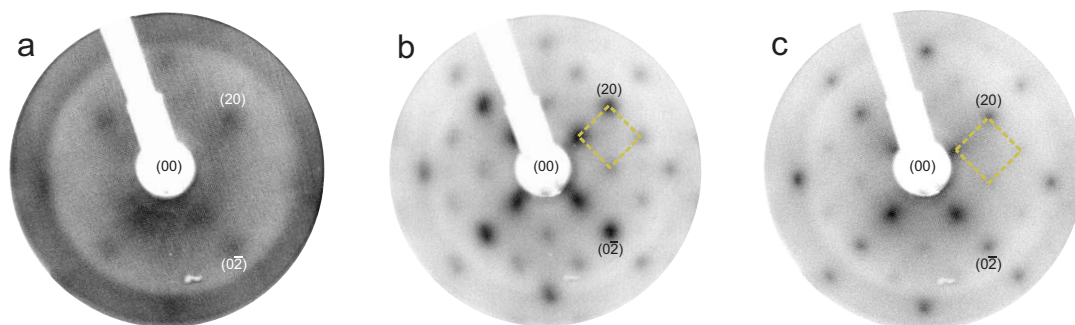


Fig. 6.5: LEED images of the sample with thin NiO interlayer at an electron energy of 128 eV after annealing steps (a) 400°C , (b) 600°C , and (c) 800°C . The dashed yellow square indicates a (1×1) 2D surface structure.

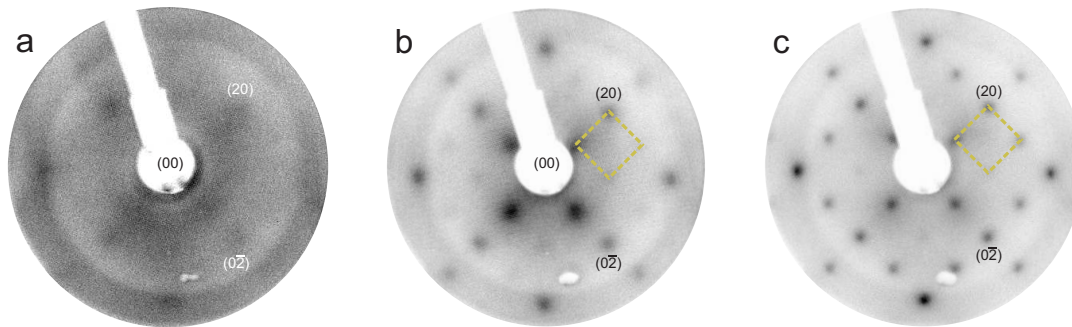


Fig. 6.6: LEED images of the sample with thick NiO interlayer at an electron energy of 128 eV after annealing steps (a) 400 °C, (b) 600 °C, and (c) 800 °C. The dashed yellow square indicates a (1×1) 2D surface structure.

images (Fig. 6.5b and Fig. 6.6b) now show bright and sharp reflex spots, confirming a clean surface and indicating a well ordered crystalline surface structure. Further annealing increases spot sharpness for the sample with thin NiO interlayer only slightly (Fig. 6.5c), while for the sample with thick NiO interlayer the spot sharpness increases clearly (Fig. 6.6c).

Analysing the spot profile of the $(0\bar{2})$ reflex confirms the observations concerning spot sharpness in the LEED images. The resulting FWHM for the $(0\bar{2})$ reflex are given in Tab. 6.2 in % of the Brillouin zone. After the second annealing step the FWHM of the $(0\bar{2})$ reflex has decreased for both samples to a significantly smaller, almost identical value, indicating a clean surface with similar crystallographic quality. For the last annealing step only a small decrease of the FWHM can be observed for the sample with thin NiO interlayer, while for the sample with thick NiO interlayer the FWHM decreases significantly, indicating a higher crystallographic order of the surface.

sample	initial	400 °C	600 °C	800 °C
thin NiO interlayer	33 ± 4	44 ± 5	36 ± 4	33 ± 4
thick NiO interlayer	34 ± 4	56 ± 6	34 ± 4	25 ± 3

Table 6.2: FWHM [%BZ] of the $(0\bar{2})$ reflex from the LEED images in Fig. 6.5 and Fig. 6.6 after successive annealing steps (initial is directly after sample preparation).

For the LEED images after the second and third annealing step, the difference in brightness of the various reflex spots changes with the electron energy, so that in total a periodicity of the LEED reflexes can be deduced, that corresponds to the (1×1) 2D surface lattice of the spinel structure. A $(\sqrt{2} \times \sqrt{2})R45$ superstructure of the magnetite surface reconstruction, as observed directly after sample preparations can not be identified.

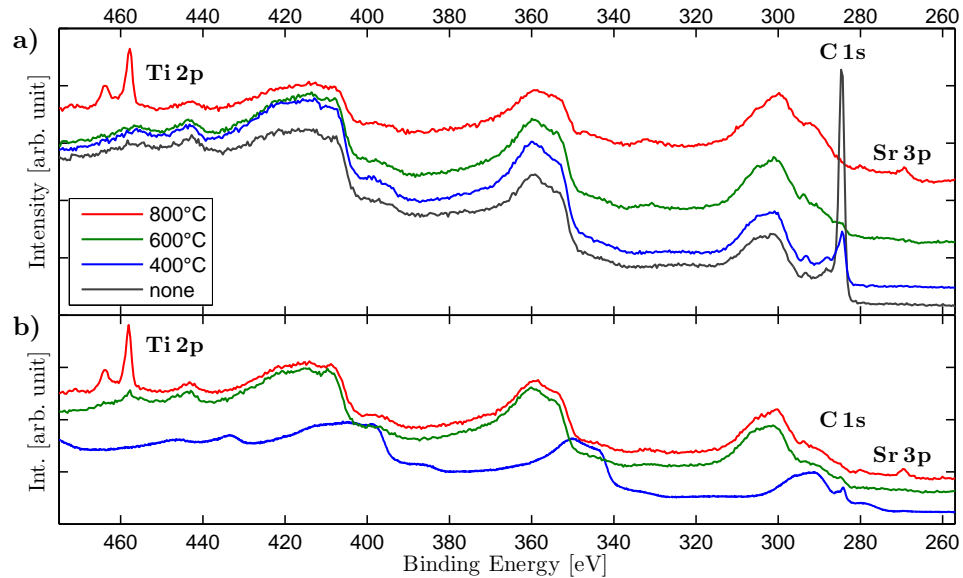


Fig. 6.7: Photoelectron spectra from the normal XPS measurements of (a) the sample with thick NiO interlayer and (b) the sample with thin NiO interlayer, after successive annealing steps. The 400 °C spectrum in (b) has been acquired with a by 10 eV smaller excitation energy, identifying the features between the Ti 2p and C 1s peaks as Fe LMM Auger peaks.

6.4 Analysis of the Surface Near Layers

For the normal XPS measurements with an excitation energy $h\nu = 1000$ eV, the information depth $ID(95\%)$ for the Ni 2p, Fe 2p and O 1s photoelectrons is 1.57 nm, 2.28 nm, and 3.15 nm, respectively. As the magnetite layer of both samples is more than 5 nm thick, it can be assumed that the XPS data of the corresponding photoelectron peaks only holds information on that layer.

The photoelectron spectra in Fig. 6.8 and Fig. 6.9 show no evident qualitative differences between the two samples. Energy calibration of the XPS data has been done using the O 1s peak at the binding energy of 530 eV. The corresponding spectra are shown in Fig. 6.8c and Fig. 6.9c. For the quantitative analysis the peak intensity has been determined by integrating over the shown energy range, subtracting the depicted Shirley background.

The spectra of the Fe 2p photoelectrons in Fig. 6.8b and Fig. 6.9b show the Fe $2p_{3/2}$ peak at a binding energy of 711 eV and the Fe $2p_{1/2}$ peak at a binding energy of 724 eV. In the spectrum before annealing and in the spectra after the 400 °C annealing step, no satellite peak is visible between the two main peaks, which indicates magnetite in the topmost layers of the samples [40]. For the spectra after the 600 °C and 800 °C annealing steps, a distinctive satellite becomes visible on the foot of the Fe $2p_{1/2}$ peak, which is typical for trivalent iron, indicating a deficiency of divalent iron in the magnetite layer. The determination of the Fe 2p peak intensity for the quantitative analysis is done by integrating over the whole range of the Fe 2p spectrum, subtracting the depicted Shirley

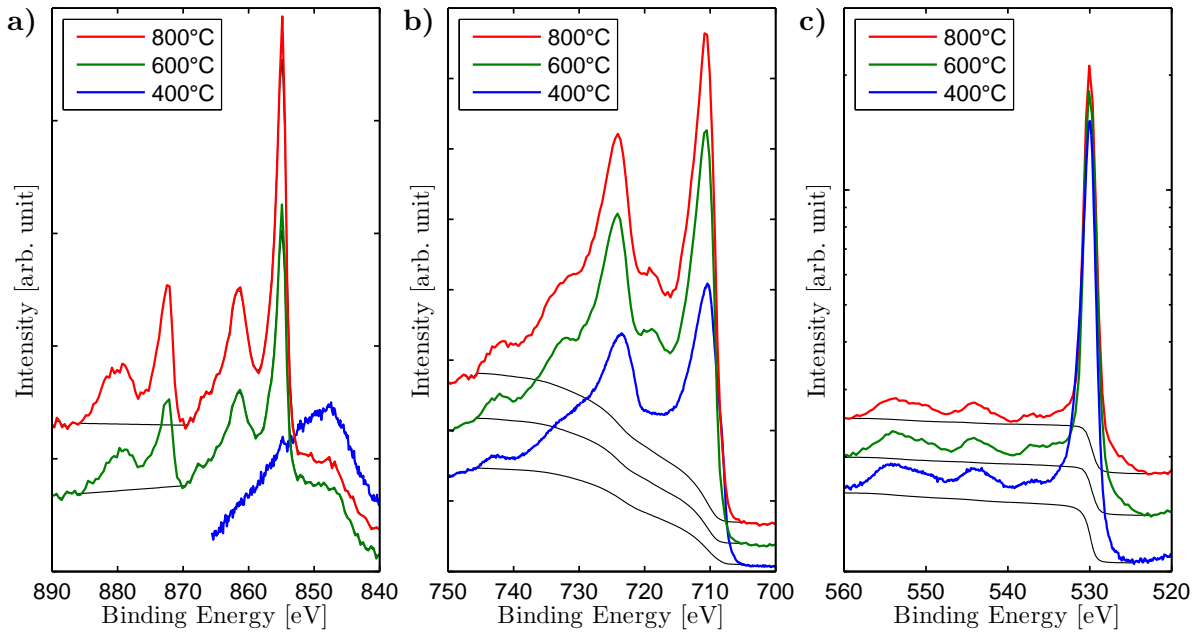


Fig. 6.8: Photoelectron spectra of the sample with thin NiO interlayer, after different annealing steps: (a) Ni 2p spectrum, (b) Fe 2p spectrum, and (c) O 1s spectrum. Thin black lines show the respectively chosen background.

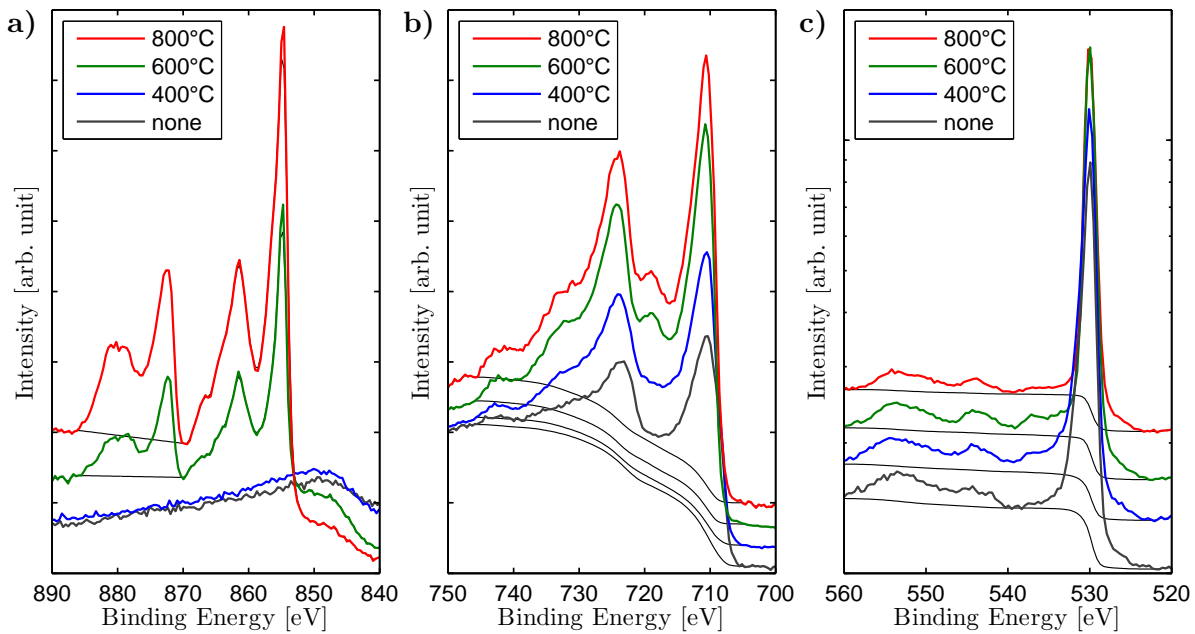


Fig. 6.9: Photoelectron spectra of the sample with thick NiO interlayer, after different annealing steps: (a) Ni 2p spectrum, (b) Fe 2p spectrum, and (c) O 1s spectrum. Thin black lines show the respectively chosen background.

background.

Fig. 6.8a and Fig. 6.9a show the spectra of the Ni 2p photoelectrons, which consist of the Ni 2p_{3/2} peak at a binding energy of 855 eV and the Ni 2p_{1/2} peak at a binding energy of 872 eV. Before the second annealing step at 600 °C, there is no Ni 2p signal visible. Only from the Fe 2s core level with a binding energy of 848 eV some wide spread intensity distribution can be observed. The photoelectron peaks of the Ni 2p core level first appear after the 600 °C annealing step and are still present after the 800 °C annealing step with no evident qualitative changes. Both of the main peaks are accompanied by relatively big plasmon loss peaks [17] on their high binding energy side. As the main Ni 2p_{3/2} peak exhibits no shoulder on its high binding energy side, the nickel spectra resemble more the reference data for nickel ferrite (NiFe₂O₄) [7] rather than that of NiO [17]. The presence of the Fe 2s peak with its highly asymmetric shape, superimposing the Ni 2p peak, complicates intensity determination for the quantitative analysis. Considering its influence on the Ni 2p_{1/2} peak as insignificantly small, the intensity of the nickel peak has been determined by only integrating over that part of the spectrum, choosing a linear background profile and weighting the intensity with the corresponding sensitivity factor.

The quantitative analysis of the XPS data evaluates intensity ratios of the Ni 2p, Fe 2p, and O 1s photoelectron peaks, in order to gain information on the stoichiometry of the magnetite layer over the course of the successive annealing steps.¹ The intensity ratios

$$\frac{I'_{\text{Fe}}}{I'_{\text{Fe}} + I'_{\text{Ni}} + I'_{\text{O}}} \text{ and } \frac{I'_{\text{Ni}}}{I'_{\text{Fe}} + I'_{\text{Ni}} + I'_{\text{O}}} \quad (6.1)$$

have been calculated according to equation (3.8) and are plotted in Fig. 6.10. For comparison, theoretically expected intensity ratios for stoichiometric proportions of iron and nickel in Fe₃O₄, FeO, and NiFe₂O₄ have been calculated after equation (3.5) and are also plotted in Fig. 6.10.

For the sample with thin NiO interlayer (Fig. 6.10a), the initial data, after the first annealing step, suggests a surplus of iron in the magnetite layer, matching the stoichiometry of FeO, rather than Fe₃O₄. This is not in agreement with the Fe 2p spectrum in Fig. 6.8b, which does not show a satellite peak for FeO. Here, a systematic error in the determination of the intensities, probably that of oxygen, might be the cause, but no solution could be found. In the next two annealing steps small amounts of nickel diffuse into the magnetite layer, while equal amounts of iron dissipate, so that the total proportion of iron and nickel stays constant. The final amounts of nickel and iron do not match those expected for NiFe₂O₄.

For the sample with thick NiO interlayer (Fig. 6.10b), the intensity ratio before annealing suggests a small deficiency of iron, while the data after the first annealing step indicates a small surplus of iron, but both values are within the margin of error still in good agreement with the expected ratio for stoichiometric Fe₃O₄. The relative increase of iron is most likely a result of a surplus of oxygen contained in the contamination

¹For simplicity, in the following the designation of the core level in Ni 2p, Fe 2p, and O 1s has been omitted.

layer on the surface of the sample before annealing, which desorbs in the first annealing step. In the second annealing step at 600 °C nickel diffuses into the magnetite layer and iron dissipates from it. The amount of nickel diffusing into the magnetite layer is much greater than compared to the diffusion in the sample with thin NiO interlayer. In the last annealing step at 800 °C even more nickel diffuses into the topmost layers, but with the amount of iron dissipating, the total amount of iron and nickel stays nearly the same within the margin of error.

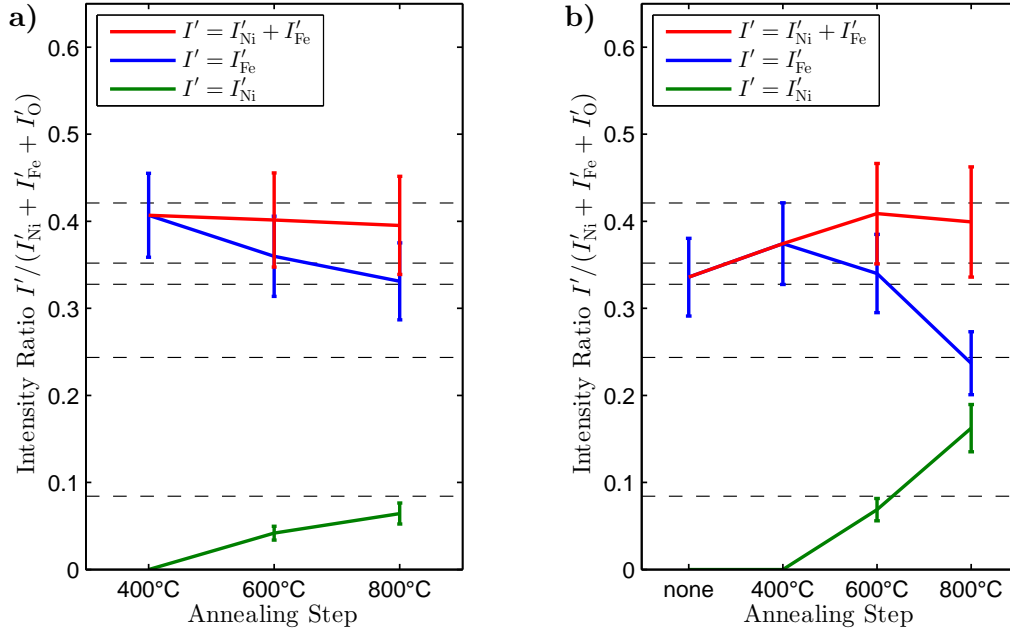


Fig. 6.10: Intensity ratios of Fe, Ni, and Fe+Ni compared to Fe+Ni+O in (a) the sample with thin NiO interlayer and (b) the sample with thick NiO interlayer, after successive annealing steps. Dashed lines indicate (from top to bottom) ratios for iron in FeO, iron in Fe₃O₄, iron plus nickel in NiFe₂O₄, iron in NiFe₂O₄ and nickel in NiFe₂O₄.

6.5 Depth Profiling

Due to the high excitation energy used in the HAXPES measurements, the resulting photoelectrons have very long IMFPs, which allows for probing of the sample down to the STO substrate. The information depth ID(95%) of the Ni 2p and Fe 2p photoelectrons in this experiment is 22 nm for photoemission normal to the surface, with little dependence on the relative small difference in kinetic energy. Analysing the photoemission at an angle relative to the surface normal of 45° and 60°, reduces the information depth to 16 nm and 11 nm, respectively, which still covers the thickness of both layers on the the samples. The idea in this experiment is, that the angular dependence in the exponential functions of equations (3.4) and (3.6) yields relatively more intensity from surface near areas with increasing angles.

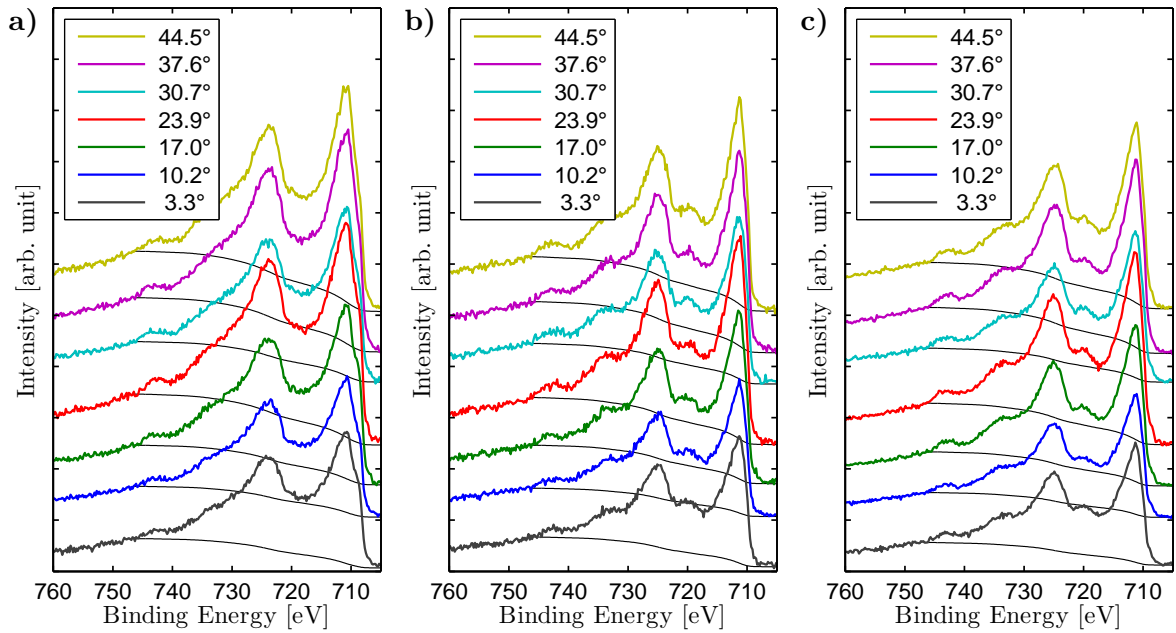


Fig. 6.11: Fe 2p spectra from HAXPES measurements of the sample with thin NiO interlayer for different angles of photoemission after (a) annealing at 400 °C, (b) annealing at 600 °C, and (c) annealing at 800 °C. Thin black lines show the respectively chosen background.

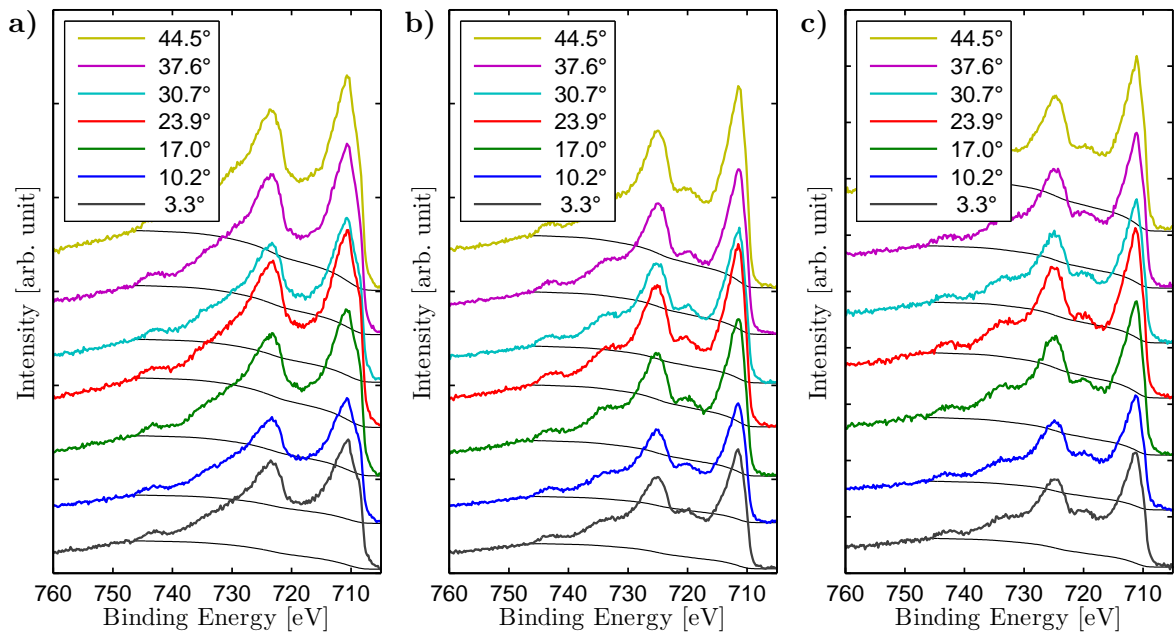


Fig. 6.12: Fe 2p spectra from HAXPES measurements of the sample with thick NiO interlayer for different angles of photoemission after (a) annealing at 400 °C, (b) annealing at 600 °C, and (c) annealing at 800 °C. Thin black lines show the respectively chosen background.

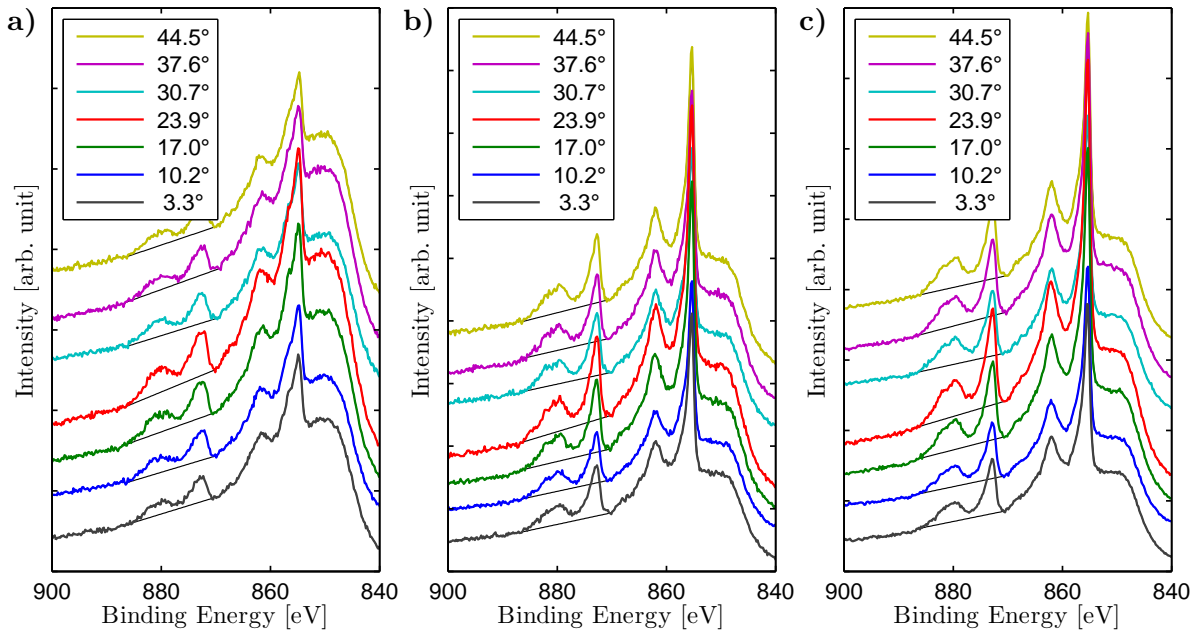


Fig. 6.13: Ni 2p spectra from HAXPES measurements of the sample with thin NiO interlayer for different angles of photoemission after (a) annealing at 400 °C, (b) annealing at 600 °C, and (c) annealing at 800 °C. Thin black lines show the respectively chosen background.

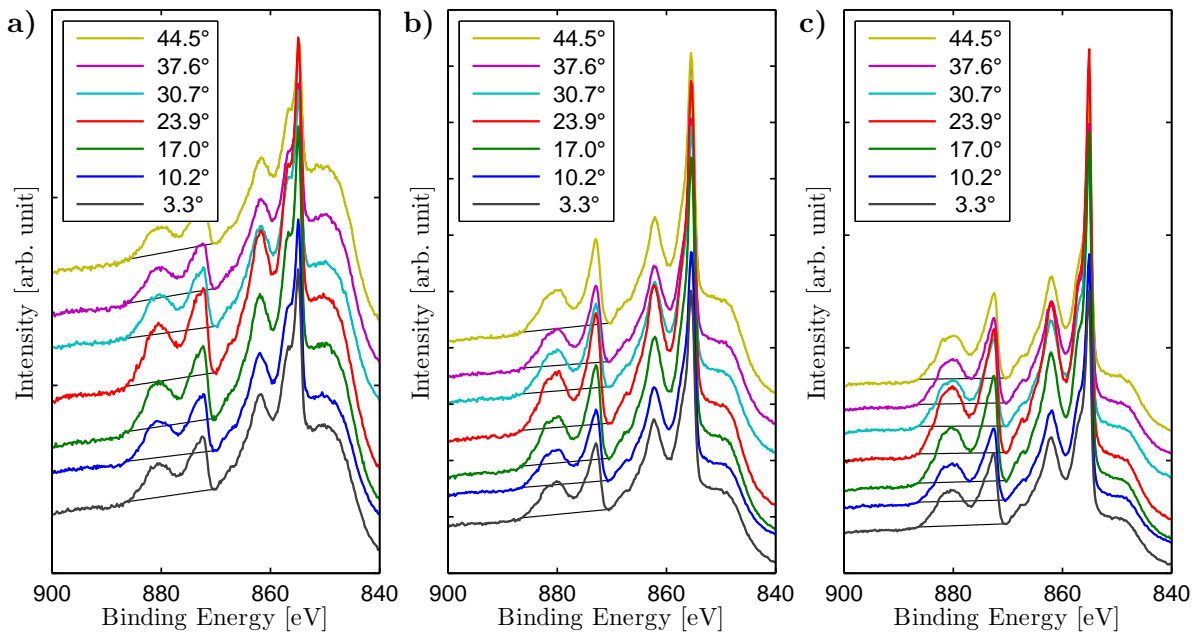


Fig. 6.14: Ni 2p spectra from HAXPES measurements of the sample with thick NiO interlayer for different angles of photoemission after (a) annealing at 400 °C, (b) annealing at 600 °C, and (c) annealing at 800 °C. Thin black lines show the respectively chosen background.

Fig. 6.11 and Fig. 6.12 show the Fe 2p spectra from the HAXPES measurements of the two samples. After the first annealing step at 400 °C, there is little qualitative difference between the spectra, as they all show the characteristic line shape of magnetite. After the second annealing step at 600 °C, the Fe³⁺ satellite becomes equally visible in all spectra, indicating a homogeneous deficiency of divalent iron in the samples, as no angular dependence can be detected. The same holds true for the third annealing step at 800 °C, as no qualitative changes of the Fe 2p spectra can be observed.

The Ni 2p spectra from the HAXPES measurements are shown in Fig. 6.13 and Fig. 6.14. After the first annealing step, the Ni 2p_{3/2} peak of the sample with thick NiO interlayer (Fig. 6.14a) clearly shows a shoulder on its high binding energy side, independent of the photoemission angle, indicating that all nickel in the sample exists in the form of NiO [17]. For the sample with thin NiO interlayer the signal intensity from nickel is very small compared to the extensive Fe 2s peak (Fig. 6.13a), so that there is much uncertainty in the interpretation of the Ni 2p spectra. At least for small photoemission angles the line shape of the spectra suggest a shoulder on the high binding energy side of the Ni 2p_{3/2} peak, indicating that there is nickel in the form of NiO present in the sample, but no definite conclusions can be made. After the second annealing step, the intensity of the Ni 2p peak from the sample with thin NiO interlayer has increased significantly. Both samples now show independent of the photoemission angle no shoulder on the Ni 2p_{3/2} peak, suggesting that most nickel in the sample is present in the form of NiFe₂O₄. For the sample with thin NiO interlayer, this does not change after the third annealing step. However, the spectra of the sample with thick NiO interlayer again show a small shoulder on the Ni 2p_{3/2} peak for the emission angles 10.2 to 37.6°. This may indicate the existence of NiO in some parts of the sample.

For the quantitative analysis of the photoelectron spectra, peak intensities of the Ni 2p and Fe 2p peak have been determined in the same way as described in section 6.4. To analyse the distribution of nickel and iron in the sample, the intensity ratio

$$\frac{I'_{\text{Ni}}}{I'_{\text{Ni}} + I'_{\text{Fe}}} \quad (6.2)$$

is formed and compared to theoretically expected behaviour. As reference, the intensity ratios for a possible initial and final state are calculated from equations (3.4) and (3.6). For the initial state two separated, stoichiometric layers of NiO and Fe₃O₄ with thickness t_{Ni} and t_{Fe} , as determined by XRR, are assumed. A probable final state of a diffusion process is an equal distribution of nickel and iron across a single layer of thickness $t_{\text{Ni}} + t_{\text{Fe}}$. The resulting functions are plotted in Fig. 6.15 together with the ratios from the experimental data. The curves of the experimental data all exhibit a regular, coinciding pattern, that does not occur in the theoretically derived functions. Because an angular dependence of the detector sensitivity has been ruled out (see section 6.2) and the curves resemble diffraction patterns, the hypothesis is made, that the photoemission process underlies the effect of photoelectron diffraction. Photoelectron diffraction is observed in XPS experiments with single crystals, where the photoelectrons are diffracted from crystal planes and their intensity is enhanced for emission parallel to crystal planes

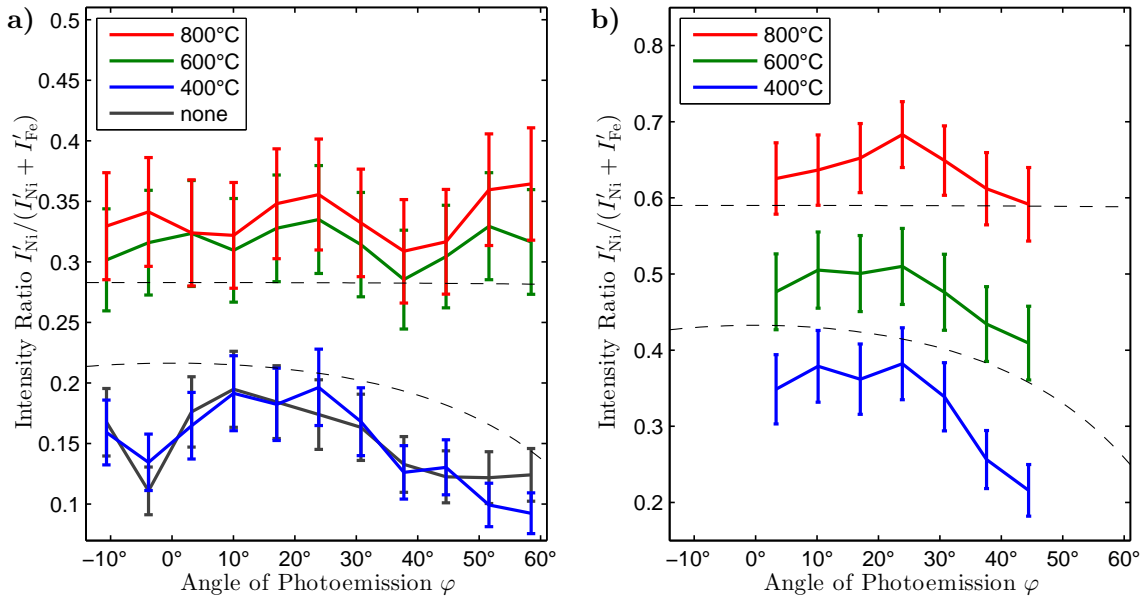


Fig. 6.15: Relative intensity of Ni compared to Fe+Ni from (a) the sample with thin NiO interlayer and (b) the sample with thick NiO interlayer, for different angles of photoemission after annealing at different temperatures (none is before annealing). Dashed lines indicate intensity for two separate layers (bottom) and one homogeneous combined layer (top).

[9]. As the theory on photoelectron diffraction goes beyond the scope of this work, the quantitative analysis is limited to the change of intensity ratios between annealing steps.

For the sample with thin NiO interlayer (Fig. 6.15a), the curves of the intensity ratio before and after the first annealing step coincide almost perfectly, indicating that annealing at 400 °C causes no diffusion in the sample. After the second annealing step, the relative intensity of the nickel signal increases, indicating diffusion of nickel towards the surface and of iron away from the surface. The third annealing step increases the intensity ratio only slightly further, suggesting that an equilibrium state has been reached. Despite the deviations due to photoelectron diffraction, the experimental data lies well in the vicinity of the theoretical curves. The intensity ratios for the sample with thick NiO interlayer (Fig. 6.15b) show a continuous increase of the nickel intensity over the annealing steps. The intensity ratio starts near the calculated values for two separate layers, ending near to the range calculated for a single layer of equally distributed nickel and iron.

Finally, the diffusion behaviour of strontium and titanium from the STO substrate is analysed. From the XPS data in Fig. 6.7 the presence of strontium and titanium in the magnetite layer can be deduced by the Sr 3p peak, located around a binding energy of 460 eV, and the Ti 2p peak, located around 270 eV, respectively. The Ti 2p peak can be clearly identified only in the spectra after the 800 °C annealing steps. Before that, only the spectrum of the sample with the thin NiO interlayer after the 600 °C annealing step shows a small spike at the Ti 2p position. Although the information depth ID(95) of the Sr 3p peak (4.29 nm) is greater than that of the Ti 2p peak (3.45 nm), only after

the 800 °C annealing steps, small spikes of the Sr 3p peak can be detected.

6.6 Discussion

The effects of post deposition annealing on Fe₃O₄/NiO double layers on STO substrates in an O₂ atmosphere of 5×10^{-6} mbar have been studied for two samples using XPS and HAXPES measurements at a synchrotron beamline, in conjunction with LEED experiments.

For the initial data acquired during sample preparation it has been shown, that two epitaxial layers have grown on both STO substrates with coinciding crystal orientation. The intermediate NiO layer has been grown in two thickness's of 1.5 nm (thin) and 5.6 nm (thick), with the thin layer showing more structural disorder in LEED images from the relaxation processes due to the lattice misfit on STO. The Fe₃O₄ layers are grown with an almost equal thickness of 5.4 nm (thin) and 5.5 nm (thick). LEED and XPS measurements have shown, that epitaxial cube-on-cube magnetite layers have formed on the NiO layers. The initial XPS and HAXPES data acquired at the synchrotron beamline confirm these results.

The first annealing step at 400 °C only has an effect on the sample surface. The LEED images and the XPS measurement directly made before annealing show that a contamination layer had formed on the samples from exposure to air. Although some residual carbon has been detected in the XPS data after the first annealing step, weak reflex spots become visible in the LEED images. The analysis of the Fe 2p and Ni 2p spectra from the XPS and HAXPES measurements still show the expected line profiles for NiO and magnetite. The evaluation of intensity ratios from both measurements show no changes that can be accounted to interdiffusion between the the two films. This suggests, that annealing at a temperature of 400 °C can be used to remove surface contamination, with so far no effects on the sample itself. XRD measurements could be used to check for structural changes.

After the second annealing step at 600 °C the distribution of nickel and iron in the sample has changed, as the intensity ratios from the XPS and HAXPES data show. It is believed, that there has been interdiffusion of nickel and iron between the NiO and Fe₃O₄ film, rather than de-wetting of the Fe₃O₄ film. This is supported by the analysis of the Fe 2p photoelectron peak profiles, that show that the ratio of divalent and trivalent iron has changed significantly from that of magnetite to a surplus of trivalent iron. Furthermore, the Ni 2p peak profiles, which initially confirmed the existence of nickel in the form of NiO, now suggest the existence of nickel ferrite (NFO).

Further annealing at 800 °C accelerates the diffusion of nickel and iron in the sample with thick NiO interlayer, while in the sample with thin NiO interlayer almost no further changes can be seen. For the sample with thin NiO interlayer an even distribution of iron and nickel is almost reached after the second annealing step, as the comparison with the theoretically expected intensity ratios indicates.

The diffusion behaviour of titanium and strontium from the STO substrate gives further evidence against de-wetting of the films. If the films fracture by the annealing

process, the XPS signals of both, titanium and strontium should increase equally. This is not observed, the titanium signal is detected more strongly than the strontium signal. For final evidence against de-wetting, AFM measurements of the samples are needed.

The overall cubic crystal structure seems to remain on a larger scale unchanged, as the LEED images after the second and third annealing step show a matching (1×1) surface structure. From the observation of photoelectron diffraction in the HAXPES data, which requires a well ordered crystal structure, this can also be confirmed for the structure below the surface. Final evidence about the crystal structure after the annealing procedure could be gained by XRR and XRD measurements.

Cornell and Schwertmann [12] mention, that in the spinel structure of magnetite the divalent iron can easily be replaced by divalent ions from other elements. The above results suggest, that non stoichiometric nickel ferrite forms in the diffusion process as a result of annealing above 400°C . The proportional amounts of nickel and iron in both samples do not match the ratio of $1 : 2$ for nickel ferrite, but are $1 : 2.6$ for the sample with thin NiO interlayer and $1 : 0.7$ for the sample with thick NiO interlayer. This discrepancy may, in the sample with thick NiO interlayer, lead to the segregation of NiO clusters. The HAXPES data suggests this, as no more signs of NiO can be detected after the second annealing step, while after the third annealing step, there are again indications for NiO.

7 Conclusion

In the first part of this work the influence of different parameters on the growth of ultrathin Fe_3O_4 films on $\text{STO}(001)$ supports have been studied. Four samples have been prepared, two with a low deposition rate and two with a high deposition rate. For each of these deposition rates, samples with deposition temperatures of 250°C and 450°C have been created. From the comparison of XPS peak intensities, layer plus island growth has been identified for the samples grown at 450°C . The samples grown at 250°C also show behaviour of layer plus island growth, but very close to the behaviour of ideal layer-by-layer growth. AFM images of the final films show massive islands on the samples grown at 450°C , while the samples grown at 250°C show many small islands. On these, the faster deposition rate increases the island density clearly. From the LEED experiments, an epitaxial $\text{Fe}_3\text{O}_4(111)$ interface layer could be identified, before epitaxial $\text{Fe}_3\text{O}_4(001)$ islands with regular, $[111]$ oriented facets start to grow. These results suggest a low sample temperature and a high deposition rate for the growth of plain Fe_3O_4 films on $\text{STO}(001)$. Further experiments on continuously grown films need to be carried out, in order to investigate the influence of the stepwise growth procedure.

In the second part of this work, the diffusion behaviour in $\text{Fe}_3\text{O}_4/\text{NiO}/\text{STO}(001)$ systems at different annealing temperatures has been studied. From XPS, HAXPES and LEED experiments, the effects of annealing in different sample depth could be analysed. The results show that annealing at a temperature of up to 400°C leads to desorption of surface contaminations, with no detectable effect on the sample itself. Annealing at higher temperatures leads to interdiffusion of Fe and Ni in the Fe_3O_4 and NiO layers. In a sample with thin NiO interlayer complete intermixing of Fe and Ni is suspected, while in a sample with thick NiO interlayer the formation of NiO clusters is suspected. The formation of NiFe_2O_4 is possible. Diffusion from the STO support is only observed for Ti at an annealing temperature of 800°C , which indicates that no de-wetting has occurred. Further studies to investigate possible structural changes could be XRR, XRD and AFM measurements.

Bibliography

- [1] Y. A. Abramov, V. G. Tsirelson, V. E. Zavodnik, S. A. Ivanov, and B. I. D. The chemical bond and atomic displacements in SrTiO₃ from x-ray diffraction analysis. *Acta Crystallographica Section B*, 51(6):942–951, 1995.
- [2] O. N. Bala Sundaram, V. Veeravazhuthi, P. Meena, and K. Tamil Selvan, editors. *Thin Film: Techniques and Applications*. Allied Publishers, 2004.
- [3] F. Bertram. Röntgenreflektometrie an ultradünnen Schichten. Master's thesis, Universität Osnabrück, 2007.
- [4] F. Bertram. Röntgenstrukturanalyse von Oxidschichten. Master's thesis, Universität Osnabrück, 2009.
- [5] F. Bertram, C. Deiter, K. Pflaum, M. Suendorf, C. Otte, and J. Wollschläger. In-situ x-ray diffraction studies on post-deposition vacuum-annealing of ultra-thin iron oxide films. *Journal of Applied Physics*, 110(10):102208, 2011.
- [6] F. Bertram, C. Deiter, O. Hoefert, T. Schemme, F. Timmer, M. Suendorf, B. Zimmermann, and J. Wollschläger. X-ray diffraction study on size effects in epitaxial magnetite thin films on MgO(001). *Journal of Physics D: Applied Physics*, 45(39):395302, 2012.
- [7] M. C. Biesinger, B. P. Payne, A. P. Grosvenor, L. W. M. Lau, A. R. Gerson, and R. S. C. Smart. Resolving surface chemical states in XPS analysis of first row transition metals, oxides and hydroxides: Cr, Mn, Fe, Co and Ni. *Applied Surface Science*, 257(7):2717–2730, 2011.
- [8] M. Birkholz. *Thin Film Analysis by X-Ray Scattering*. WILEY-VCH Verlag GmbH & Co. KGaA, Weinheim, 2006.
- [9] D. Briggs and M. P. Seah, editors. *Practical Surface Analysis by Auger and X-ray Photoelectron Spectroscopy*. John Wiley & Sons, 1983.
- [10] S. A. Chambers and S. A. Joyce. Surface termination, composition and reconstruction of Fe₃O₄(001) and γ -Fe₂O₃(001). *Surface Science*, 420(2–3):111–122, 1999.
- [11] Y. Z. Chen, J. R. Sun, Y. N. Han, X. Y. Xie, J. Shen, C. B. Rong, S. L. He, and B. G. Shen. Microstructure and magnetic properties of strained Fe₃O₄ films. *Journal of Applied Physics*, 103(7):07D703, 2008.

- [12] R. M. Cornell and U. Schwertmann. *The Iron Oxides*. WILEY-VCH Verlag GmbH & Co. KGaA, Weinheim, 2 edition, 2003.
- [13] S. L. Dudarev, G. A. Botton, S. Y. Savrasov, C. J. Humphreys, and A. P. Sutton. Electron-energy-loss spectra and the structural stability of nickel oxide: An LSDA1U study. *Physical Review B*, 57(3):1505–1509, 1998.
- [14] Y. Gao, Y. J. Kim, and S. A. Chambers. Preparation and characterization of epitaxial iron oxide films. *Journal of Materials Research*, 13(07):2003–2014, 1998.
- [15] G. Gottstein. *Physical Foundations of Material Science*. Springer-Verlag Berlin Heidelberg, 2004.
- [16] A. P. Grosvenor, B. A. Kobe, M. C. Biesinger, and N. S. McIntyre. Investigation of multiplet splitting of Fe 2p XPS spectra and bonding in iron compounds. *Surface and Interface Analysis*, 36(12):1564–1574, 2004.
- [17] A. P. Grosvenor, M. C. Biesinger, R. S. C. Smart, and N. S. N. Stewart McIntyre. New interpretations of XPS spectra of nickel metal and oxides. *Surface Science*, 600(9):1771–1779, 2006.
- [18] S. Hofmann. *Auger- and X-Ray Photoelectron Spectroscopy in Materials Science*, volume 49 of *Springer Series in Surface Sciences*. Springer-Verlag Berlin Heidelberg, 2013.
- [19] I. Horcas, R. Fernández, J. M. Gómez-Rodríguez, J. Colchero, J. Gómez-Herrero, and A. M. Baro. WSXM: A software for scanning probe microscopy and a tool for nanotechnology. *Review of Scientific Instruments*, 78(1):013705, 2007.
- [20] S. Ikeda, J. Hayakawa, Y. M. Lee, F. Matsukura, Y. Ohno, T. Hanyu, and H. Ohno. Magnetic tunnel junctions for spintronic memories and beyond. *IEEE Transactions on Electron Devices*, 54(5):991–1002, 2007.
- [21] D. A. King and D. P. Woodruff, editors. *Growth and Properties of Ultrathin Epitaxial Layers*, volume 8 of *The Chemical Physics of Solid Surfaces*. Elsevier Science B.V., 1997.
- [22] G. W. Leung, M. E. Vickers, R. Yu, and M. G. Blamire. Epitaxial growth of Fe_3O_4 (111) on $SrTiO_3$ (001) substrates. *Journal of Crystal Growth*, 310:5282–5286, 2008.
- [23] F. Marhoun and Y. Kanji. High quality $Fe_3\text{-}deltaO_4/InAs$ hybrid structure for electrical spin injection. *Applied Physics Letters*, 90(11):112501, 2007.
- [24] J. T. Newberg, D. E. Starr, S. Yamamoto, S. Kaya, T. Kendelewicz, E. R. Mysak, S. Porsgaard, M. B. Salmeron, G. E. Brown Jr., A. Nilsson, and H. Bluhm. Formation of hydroxyl and water layers on MgO films studied with ambient pressure XPS. *Surface Science*, 605(1–2):89–94, 2011.

-
- [25] K. Oura, V. G. Lifshits, A. A. Saranin, A. V. Zotov, and M. Katayama. *Surface Science: An Introduction*. Advanced Texts in Physics. Springer-Verlag Berlin Heidelberg New York, 2003.
- [26] G. Pacchioni and S. Valeri, editors. *Oxide Ultrathin Films: Science and Technology*. Wiley-VCH, 2012.
- [27] C. J. Powell and A. Jablonski. Surface sensitivity of x-ray photoelectron spectroscopy. *Nuclear Instruments and Methods in Physics Research Section A: Accelerators, Spectrometers, Detectors and Associated Equipment*, 601(1–2):54–65, 2009.
- [28] C. J. Powell and A. Jablonski. *NIST Electron Inelastic-Mean-Free-Path Database*. National Institute of Standards and Technology, Gaithersburg, MD, 2010. Version 1.2.
- [29] J. H. Scofield. Hartree-Slater subshell photoionization cross-sections at 1254 and 1487 eV. *Journal of Electron Spectroscopy and Related Phenomena*, 8:129–137, 1976.
- [30] D. A. Shirley. High-resolution x-ray photoemission spectrum of the valence bands of gold. *Physical Review B*, 5(12):4709–4714, 1972.
- [31] R. Takahashi, H. Misumi, and M. Lippmaa. Growth temperature effect on the structural and magnetic properties of Fe₃O₄ films grown by the self-template method. *Journal of Applied Physics*, 116(033918), 2014.
- [32] R. Takahashi, H. Misumi, T. Yamamoto, and M. Lippmaa. Spontaneous growth of strain-free magnetite nanocrystals via temperature-driven dewetting. *Crystal Growth & Design*, 14:1264–1271, 2014.
- [33] S. Tanuma, C. J. Powell, and D. R. Penn. Calculation of electron inelastic mean free paths (IMFPs) VII. reliability of the TPP-2M IMFP predictive equation. *Surface and Interface Analysis*, 35(3):268–275, 2003.
- [34] M. B. Trzhaskovskaya, V. I. Nefedov, and V. G. Yarzhemsky. Photoelectron angular distribution parameters for elements Z=1 to Z=54 in the photoelectron energy range 100–5000 eV. *Atomic Data and Nuclear Data Tables*, 77(1):97–159, 2001.
- [35] K. van Benthem, C. Elsässer, and R. H. French. Bulk electronic structure of SrTiO₃: Experiment and theory. *Journal of Applied Physics*, 90(12):6156–6164, 2001.
- [36] F. C. Voegt, T. T. M. Palstra, L. Niesen, O. C. Rogojanu, M. A. James, and T. Hibma. Superparamagnetic behavior of structural domains in epitaxial ultrathin magnetite films. *Physical Review B*, 57(14):8107–8110, 1998.
- [37] C. D. Wagner, W. M. Riggs, L. E. Davis, and J. F. Moulder. *Handbook of X-ray Photoelectron Spectroscopy*. Perkin-Elmer Corporation, Physical Electronics Division, 1979.

- [38] K. Wasa, M. Kitabatake, and H. Adachi. *Thin film materials technology: sputtering of control compound materials*. Springer-Verlag GmbH & Co. KG, 2004.
- [39] S. A. Wolf, D. D. Awschalom, R. A. Buhrman, J. M. Daughton, S. von Molnár, M. L. Roukes, A. Y. Chtchelkanova, and D. M. Treger. Spintronics: A spin-based electronics vision for the future. *Science*, 294(5546):1488–1495, 2001.
- [40] T. Yamashita and P. Hayes. Analysis of XPS spectra of Fe²⁺ and Fe³⁺ ions in oxide materials. *Applied Surface Science*, 254(8):2441–2449, 2008.

Erklärung über die Eigenständigkeit der erbrachten wissenschaftlichen Leistung

Ich erkläre hiermit, daß ich die vorliegende Arbeit ohne unzulässige Hilfe Dritter und ohne Benutzung anderer als der angegebenen Hilfsmittel angefertigt habe. Die aus anderen Quellen direkt oder indirekt übernommenen Daten und Konzepte sind unter Angaben der Quelle gekennzeichnet.

Bei der Auswahl und Auswertung folgenden Materials haben mir die nachstehend aufgeführten Personen in der jeweils beschriebenen Weise entgeltlich/unentgeltlich geholfen:

1. _____

2. _____

3. _____

Weitere Personen waren an der inhaltlichen materiellen Erstellung der vorliegenden Arbeit nicht beteiligt. Insbesondere habe ich hierfür nicht die entgeltliche Hilfe von Vermittlungs- bzw. Beratungsdiensten (Promotionsberater oder andere Personen) in Anspruch genommen. Niemand hat von mir unmittelbar oder mittelbar geldwerte Leistungen für Arbeiten erhalten, die im Zusammenhang mit dem Inhalt der vorgelegten Dissertation stehen.

Die Arbeit wurde bisher weder im In- noch im Ausland in gleicher oder ähnlicher Form einer anderen Prüfungsbehörde vorgelegt.

Ort, Datum

Unterschrift